AGU PUBLICATIONS

JGR

Journal of Geophysical Research: Atmospheres

RESEARCH ARTICLE

10.1002/2014JD022969

This article is a companion to *Pavolonis et al.* [2015] doi:10.1002/2014JD022968.

Key Points:

- The Spectrally Enhanced Cloud Objects (SECO) algorithm was developed
- The SECO method can be applied to nearly any satellite sensor
- The SECO approach significantly improves satellite-based ash and dust detection

Correspondence to:
M. J. Pavolonis,
Mike.Pavolonis@noaa.gov

Citation:
Pavolonis, M. J., J. Sieglaff, and J. Cintineo (2015), Spectrally Enhanced Cloud Objects—A generalized framework for automated detection of volcanic ash and dust clouds using passive satellite measurements: 2. Cloud object analysis and global application, *J. Geophys. Res. Atmos.*, *120*, 7842–7870, doi:10.1002/2014JD022969.

Received 9 DEC 2014
Accepted 5 JUN 2015
Accepted article online 11 JUN 2015
Published online 11 AUG 2015

The copyright line for this article was changed on 23 SEP 2015 after original online publication.

©2015. The Authors.
This is an open access article under the terms of the Creative Commons Attribution-NonCommercial-NoDerivs License, which permits use and distribution in any medium, provided the original work is properly cited, the use is non-commercial and no modifications or adaptations are made.

Spectrally Enhanced Cloud Objects—A generalized framework for automated detection of volcanic ash and dust clouds using passive satellite measurements: 2. Cloud object analysis and global application

Michael J. Pavolonis[1], Justin Sieglaff[2], and John Cintineo[2]

[1]National Oceanic and Atmospheric Administration Center for Satellite Applications and Research, Madison, Wisconsin, USA, [2]Cooperative Institute for Meteorological Satellite Studies, Madison, Wisconsin, USA

Abstract A new approach for quantitatively detecting volcanic ash and dust from satellite has been developed. The Spectrally Enhanced Cloud Objects (SECO) algorithm utilizes a combination of radiative transfer theory, a statistical model, and image processing techniques to identify volcanic ash and dust clouds in satellite imagery with a very low false alarm rate. This fully automated technique is globally applicable (day and night) and can be adapted to a wide range of low Earth orbit and geostationary satellite sensors or even combinations of satellite sensors. The SECO algorithm consists of four primary components: conversion of satellite measurements into robust spectral metrics, application of a Bayesian method to estimate the probability that a given satellite pixel contains volcanic ash and/or dust, construction of cloud objects, and the selection of cloud objects deemed to have the physical attributes consistent with volcanic ash and/or dust clouds. The first two components of the SECO algorithm were described in Part 1 of this study. The final two components are described in this paper. In addition, case studies and a global analysis are utilized to illustrate the benefits of the SECO approach relative to the traditional "split window" ash/dust detection technique. The SECO algorithm can form the basis for more advanced applications such as volcanic cloud alerting and data assimilation.

1. Introduction

A fully automated, satellite-based, volcanic ash and dust detection technique, known as the Spectrally Enhanced Cloud Objects (SECO) algorithm, is developed. The development of the SECO algorithm is motivated by the lack of a highly skilled, globally applicable, automated volcanic ash and dust detection technique that can be applied to nearly any geostationary or low Earth orbit satellite sensor with infrared measurement capabilities day or night [*Pavolonis et al.*, 2015]. The SECO algorithm is designed to identify volcanic ash and dust in manner that is more consistent with human expert interpretation of multispectral satellite imagery than traditional techniques. The SECO approach does not attempt to distinguish between volcanic ash and dust because they generally have very similar spectral signatures at the wavelengths utilized by the SECO algorithm.

In Part 1 of this paper [*Pavolonis et al.*, 2015], several sophisticated multispectral satellite metrics, derived from measurements with central wavelengths of approximately 0.65, 3.9, 7.3, 8.5, 11, and 12 μm, were utilized in a naïve Bayesian procedure to determine the probability that a given satellite pixel contains volcanic ash and/or nonvolcanic dust. The Bayesian method can utilize all of those spectral channels or several different channel subsets as dictated by sensor capabilities, solar zenith angle, and/or intellectual curiosity [see *Pavolonis et al.*, 2015, Table 1]. The Bayesian method was trained empirically using a very large Moderate Resolution Imaging Spectroradiometer (MODIS)-based data set where the horizontal bounds of volcanic ash and dust clouds were manually analyzed. Analysis showed that the Bayesian method was skilled at distinguishing between volcanic ash/dust features and all other features (e.g., the probability was generally much greater inside actual volcanic ash and dust clouds than outside), much more so than the traditional "split window" method [e.g., *Prata*, 1989a, 1989b] technique, even when spectral channel subsets were used. The traditional split window method consists of computing the difference in brightness temperature between measurements taken at approximately 11 and 12 μm and applying a threshold. Volcanic ash and dust typically absorb, and hence emit, more radiation at 11 μm than 12 μm, resulting in a split window

brightness temperature difference that is less than 0 K in the absence of competing absorption/emission/reflection effects at those wavelengths. Conversely, liquid water and ice clouds, generated by meteorological processes (meteorological clouds), typically have a split window brightness temperature difference that is greater than 0 K. Thus, a split window threshold of about 0 K is typically used for ash/dust detection. Unfortunately, competing absorption/emission/reflection effects and measurement errors greatly limit the accuracy of the split window technique.

A human-like (i.e., high probability of detection with an extremely low false alarm rate) capability for distinguishing volcanic and dust from all other features is needed for advanced, automated applications such as volcanic eruption alerting and data assimilation. Despite the success of the pixel-level Bayesian method, it, alone, is not sufficient to produce a human-like deterministic volcanic ash/dust assessment by simply applying a probability threshold. The Bayesian method must be combined with advanced spatial analysis to produce such a result. In this paper, we will describe the remaining components of the SECO algorithm that utilize advanced spatial analysis and demonstrate that the results are consistent with human expert interpretation of multispectral satellite imagery, especially with respect to false alarm rate. Data from the MODIS are used to introduce the remaining components of the SECO algorithm and assess the impact of using various spectral channel subsets. In addition, results generated using a geostationary sensor with different measurement capabilities than MODIS are presented.

2. Review of Multispectral Parameters

In *Pavolonis et al*. [2015] (hereafter P15), several advanced multispectral parameters were introduced and subsequently utilized in the naïve Bayesian method for determining the probability that volcanic ash and/or dust is present in a given satellite pixel. These parameters and the underlying physical concepts are also invoked in this paper, so a brief review is given here. The multispectral infrared measurements were generally expressed as β ratios, as opposed to traditional brightness temperature differences (BTDs), because β ratios provide increased sensitivity to cloud microphysical properties, including cloud composition [*Pavolonis*, 2010]. As shown in equation (1), a β ratio is simply the ratio of effective (scattering is implicitly accounted for) absorption optical depth at two different wavelengths.

$$\beta(\lambda_1,\lambda_2) = \frac{\ln[1-\varepsilon_{\mathrm{eff}}(\lambda_1)]}{\ln[1-\varepsilon_{\mathrm{eff}}(\lambda_2)]} = \frac{\tau_{\mathrm{eff}}(\lambda_1)}{\tau_{\mathrm{eff}}(\lambda_2)} \tag{1}$$

The effective absorption optical depth for a given wavelength [$\tau_{\mathrm{eff}}(\lambda)$] is easily computed from the effective cloud emissivity [$\varepsilon_{\mathrm{eff}}(\lambda)$] (see equation (1)), but computation of $\varepsilon_{\mathrm{eff}}(\lambda)$ requires knowledge of the clear-sky top of atmosphere radiance and transmittance (integrated radiance and transmittance from the surface or a given atmospheric level to the top of the atmosphere) combined with the effective cloud height (and the corresponding effective cloud temperature). The clear-sky transmittance and radiance are determined using the methods described in *Heidinger and Pavolonis* [2009], *Pavolonis* [2010], *Pavolonis et al*. [2013], and P15. The effective height ("radiative center") of the cloud is unknown, so β ratios are computed using the "top of troposphere" and "opaque" cloud assumptions as described in P15. The top of troposphere β ratio, $\beta_{\mathrm{tot}}(\lambda_1, \lambda_2)$, is computed by assuming that the cloud radiative center is located at the top of the troposphere. The "opaque cloud" β ratio, $\beta_{\mathrm{opaque}}(\lambda_1, \lambda_2)$, is computed by assuming that the cloud radiative center is located at the highest level of the troposphere that results in $\varepsilon_{\mathrm{eff}}(\lambda_1)$ or $\varepsilon_{\mathrm{eff}}(\lambda_2)$ being equal to 0.98 (using equation (1) in P15). As shown in P15, β_{tot}(12 μm, 11 μm), β_{opaque}(12 μm, 11 μm), β_{tot}(8.5 μm, 11 μm), and β_{tot}(7.3 μm, 11 μm) are particularly useful for discriminating volcanic ash and dust from other features. In addition, the 11 μm effective cloud emissivity, computed using the top of troposphere assumption [$\varepsilon_{\mathrm{tot}}$ (11 μm)], is a good indicator of how much the observed radiance deviates from the estimated clear-sky radiance. Such information is important for correctly interpreting multispectral signatures related to cloud composition.

In addition to the infrared-based metrics, useful information on cloud composition can also be gleaned from visible (daytime only) and near-infrared (day and night) observations that are available on nearly every meteorological satellite sensor. When the solar zenith angle is less than 85° and sunglint is not pronounced, the ratio of the 3.9 μm reflectance and the 0.65 μm reflectance [ρ(3.9 μm, 0.65 μm) = ref [3.9 μm]/ref[0.65 μm]] is used in combination with split window (11 and 12 μm) observations to enhance

the spectral contrast between volcanic ash/dust and all other features (see *Pavolonis et al*. [2006] and P15 for a more detailed description). At solar zenith angles greater than 90°, and in the absence of stray light influences (significant sunlight impinging on the sensor when the solar zenith angle exceeds 90°), the 3.9 μm pseudoemissivity [ε_p(3.9 μm)] is used in conjunction with split window measurements to help identify ash and dust clouds. The ε_p(3.9 μm) parameter is simply defined as the ratio of the measured 3.9 μm radiance to the estimated 3.9 μm blackbody radiance [$\varepsilon_p(3.9\,\mu m) = R(3.9\,\mu m])/R_{bb}(3.9\,\mu m)$] (see *Heidinger et al*. [2012] and P15 for more information). The spatial standard deviation of the 11 μm brightness temperature [BT_{sdev}(11 μm)] and the 0.65 μm reflectance [ref_{sdev}(0.65 μm)] are also utilized as metrics in an effort to mitigate cloud edge-related measurement errors (e.g., small band to band coregistration errors can have a large impact in regions with sharp spatial gradients). The standard deviations are computed using a 3 × 3 pixel window centered on the pixel of interest.

3. Review of Ash/Dust Cloud Property Retrieval

The remaining components of the SECO algorithm also leverage information on retrieved cloud properties and their associated uncertainty. The *Pavolonis et al*. [2013] optimal estimation retrieval algorithm is applied to all satellite pixels that either have an ash/dust probability that exceeds 1.0×10^{-6}% or an 11–12 μm BTD that is less than 0 K. The retrieved mass loading and the uncertainty in the retrieved cloud emissivity, expressed as the ratio of the 1 sigma retrieval uncertainty to the a priori uncertainty, are useful for assessing the impact a given pixel will have on the total mass of ash and/or dust computed from a collection of pixels. While the methodology described in *Pavolonis et al*. [2013] requires measurements at 11, 12, and 13.3 μm, the retrieval algorithm is flexible and can be applied without the 13.3 μm channel, which is not available on many satellite sensors.

4. Cloud Object Analysis

The majority of volcanic ash and dust clouds are composed of a small subset of pixels that are spectrally unique (i.e., very unlikely to be associated with any other feature) and a larger subset of pixels that, to varying degrees, are spectrally nonunique (i.e., can sometimes be associated with other features). When very few spectrally unique pixels are present, as is common in well-dispersed ash and dust clouds, it is very difficult to achieve a useful probability of detection without significantly increasing the false alarm rate. One of the aims of the SECO algorithm is to associate spectrally nonunique pixels with the correct feature (ash/dust versus everything else) through spatial connectivity with spectrally unique pixels. In order to achieve this goal, cloud objects are constructed. In the SECO algorithm, a cloud object is defined as a collection of spatially connected satellite pixels that meet certain criteria. The methodology described in *Wielicki and Welch* [1986] is used to efficiently construct cloud objects in a single pass through the data. In Wielicki and Welch, a cloud is deemed unique when it has no edge pixels adjacent to another cloud. The cloud object procedure also allows for diagonal spatial connectivity between two pixels, and no constraints are placed on the size of cloud objects. The most challenging aspect of the cloud object generation procedure is establishing which pixels are suitable for inclusion into cloud objects. The volcanic ash/dust probability determined using the methods described in P15 plays a critical role in constructing cloud objects and interpreting cloud object properties.

4.1. Cloud Object Membership

As shown in P15, the volcanic ash/dust probability, while generally quite skillful, does not always provide robust separation from nonash/nondust features. In other words, there are instances where high probabilities are associated with nonash/nondust features and low probabilities are associated with ash/dust features. The lack of separation is generally caused by a combination of ambiguity in the multispectral signature of ash/dust (other surface and atmospheric features sometimes have a very similar spectral signature as volcanic ash and dust) and uncertainty in the clear-sky radiative transfer required to construct our advanced spectral metrics. Measurement errors can also be problematic. Over land, complexities related to surface temperature and emissivity can further increase the overlap of the probability distributions derived from observations inside and outside of the volcanic ash/dust cloud. Thus, determination of cloud object membership using a simple probability threshold is not optimal.

In lieu of a single probability threshold, the probability information is combined with several other variables to determine which pixels can belong to a cloud object. The cloud object selection criteria options were developed heuristically using physical reasoning. Given the extremely large size of the data set used to train the Bayesian method, development of objective multivariate selection criteria was impractical. The cloud object membership criteria options are based on the following physical reasoning. Larger (more conservative) volcanic ash/dust probability thresholds should be utilized when the observed 11 μm radiance deviates very little from the clear-sky value (e.g., ε_{tot}(11 μm) is small) *and* the observed 11–12 μm BTD does not exhibit, at the very least, a semirobust ash/dust signature *and* the calculated clear-sky minus the observed 11–12 μm BTD (hereafter referred to as BTD_Bias) is small *and* the uncertainty in the retrieved cloud emissivity is large (meaning that addition of this pixel to the cloud object will add significant uncertainty to the total mass of volcanic ash or dust in the cloud object). Local spatial contrast metrics are also used in the cloud object membership decision-making process, and extra consideration (the probability threshold is lowered) is given to pixels that exhibit an SO_2 signal (SO_2 and volcanic ash are often, though not always, collocated). All pixels that have an ash/dust probability that exceeds at least one of the thresholds computed using the functions in Appendix A are allowed to be part of a cloud object.

Figure 1 helps demonstrate how the cloud object construction process works. A volcanic ash cloud (with SO_2) from the 20 February 2001 eruption of Mount Cleveland in the Aleutian Islands (Alaska) can be seen in the false color images shown in Figures 1a–1c. The approximate horizontal boundary of the ash cloud, determined through manual analysis of the false color imagery, is overlaid in white. The cloud boundary contour is also referred to as the region of interest (ROI), as ROI software is used in the manual analysis process. Interpretation of the false color imagery, including imagery for this particular case, is discussed in detail in *Pavolonis* [2014] and P15 and, in general, in *Lensky and Rosenfeld* [2008]. The volcanic ash/dust probability computed using the multispectral Bayesian method described in P15 is shown in Figure 1d. As described in P15, the naïve Bayesian method for determining the probability is not applied to pixels that clearly lie outside of theoretical constraints defined by β_{tot}(12 μm, 11 μm) (when the ash/dust probability is not computed, the corresponding 11 μm image is shown). The end result of sorting eligible pixels into cloud objects is show in Figure 1d by imaging the median ash/dust probability of the pixels that compose the object. More specifically, the median probability of the object is assigned to each pixel in the object (e.g., the same color associated with a given median object probability is assigned to each pixel in the object) as shown in Figure 1e. While many pixels with a valid probability do not meet the object membership criteria, several cloud objects of various sizes are constructed inside and outside of the ROI. The volcanic ash cloud shown in Figure 1 is fairly well dispersed and, as such, is composed entirely of optically thin cloud elements (P15). In some regions of the volcanic ash cloud, the optical depth of the cloud for a given set of conditions falls below the quantitative detection limit (the presence of ash in some regions is primarily inferred through spatial deduction), resulting in multiple cloud objects within the ROI. Note, however, that the cloud objects within the ROI generally have a much greater median probability than the objects outside of the ROI. In addition, the pixels selected for cloud object membership need not have a robust traditional split window signal. In fact, many of the pixels retained for further analysis have *positive* 11–12 μm BTD (see Figure 1c). Retaining pixels with positive 11–12 μm BTD is critical because there are several factors that can cause volcanic ash/dust to have positive 11–12 μm BTD (e.g., water vapor absorption, underlying or collocated liquid water or ice particles, large particle sizes, and rock type). The β ratio parameters used in the naïve Bayesian approach account for factors such as water vapor and surface emission that, at times, causes the split window BTD to be positive. These factors are accounted for through the calculation of the expected clear-sky radiance in each satellite channel.

4.2. Cloud Object Statistics

Several key cloud object properties are used to determine if a given cloud object, and all of the pixels that compose the object, are part of an actual volcanic ash or dust cloud. More specifically, the cloud object size (in pixel counts), median volcanic ash/dust probability of pixels within the object, cloud object probability, and spectral robustness ratings are utilized by the cloud object selection procedure. The size of the cloud object and the median pixel probability are trivial to calculate and require no further explanation. The remaining two object properties are described in greater detail.

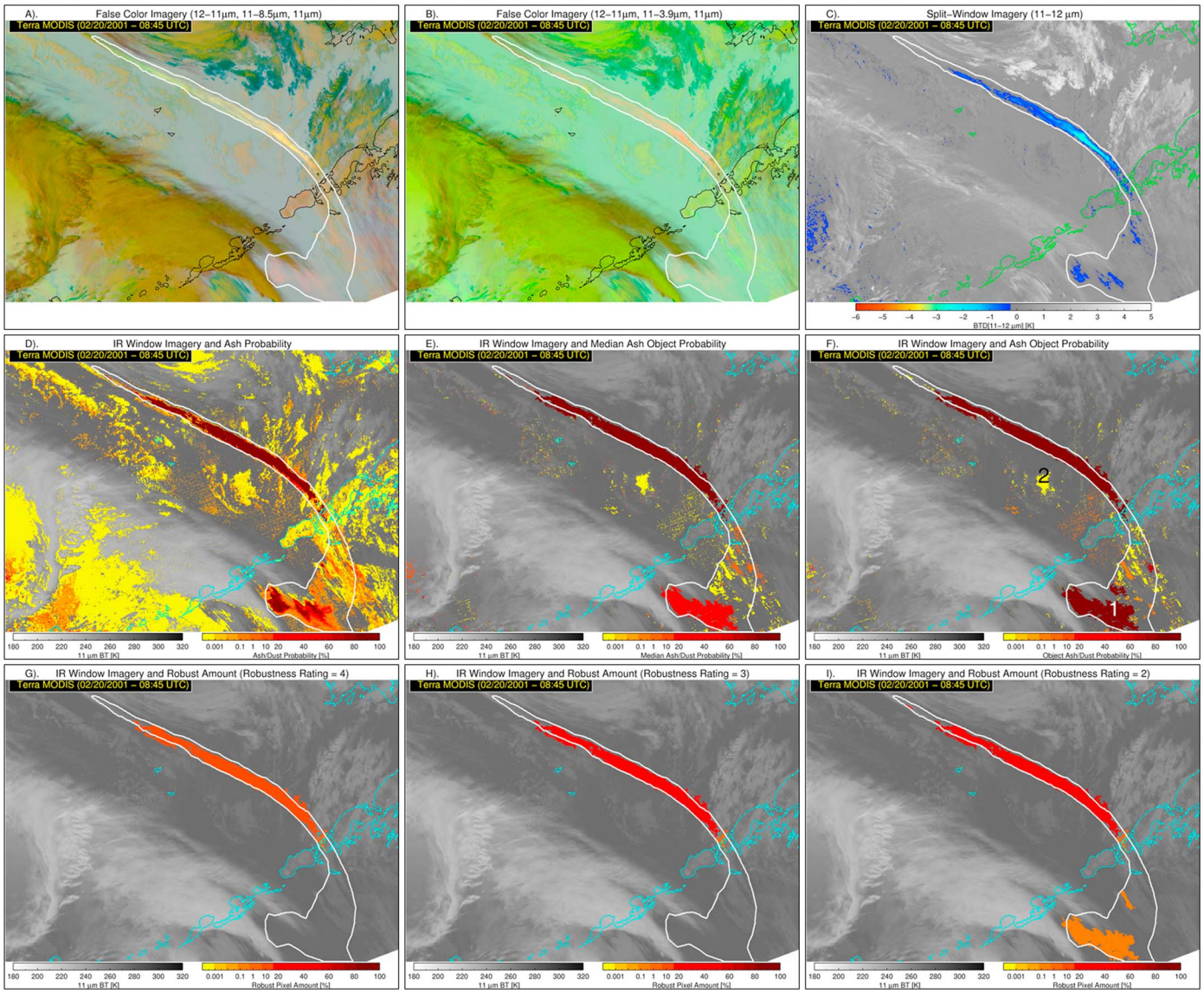

Figure 1. Images of the primary metrics utilized to construct cloud objects and apply a binary ash/dust classifier to each cloud object are shown. All parameters were derived from a nighttime Terra MODIS image from 20 February 2001 at 08:45 UTC. The approximate visual bounds of a volcanic ash cloud produced by an eruption of Mount Cleveland (Alaska) are overlaid on each image in white. (a) 12–11 μm, 11–8.5 μm, and 11 μm false color image. (b) 12–11 μm, 11–3.9 μm, and 11 μm false color image. (c) Image of BTD(11–12 μm). (d) Ash/dust pixel probability image. (e) Median ash/dust probability of pixels that compose each cloud object. (f) The probability that the cloud object is part of a volcanic ash/dust cloud. (g) The fraction of cloud object pixels that have a spectrally robust ash/dust signature using the most strict definition of spectral robustness. (h) The fraction of cloud object pixels that have a spectrally robust ash/dust signature using the second most strict definition of spectral robustness. (i) The fraction of cloud object pixels that have a spectrally robust ash/dust signature using the third strictest definition of spectral robustness. In Figures 1d–1i the 11 μm brightness temperature image is shown when the variable of interest is invalid. Two objects of interest are labeled 1 and 2 in Figure 1f. The 3.9, 7.3, 8.5, 11, and 12 μm channels were used to generate these results.

The cloud object probability is defined as the probability that a given cloud object is, itself, an ash/dust cloud or is part of a larger ash/dust cloud. The cloud object probability addresses the following question. Given a collection of spatially connected satellite pixels, what is the probability that the resulting spatially aggregated multispectral signature is associated with volcanic ash or dust? This differs from the median probability metric that quantifies the extent to which individual pixels in the object have a spectral signature that is associated with volcanic ash or dust. This concept is best explained using an example. Suppose that a large (1000 pixels or greater) cloud object is composed primarily of pixels that have a weak to moderate volcanic ash/dust multispectral signature such that the probability that a given individual pixel contains volcanic ash or dust is, at most, 50%. The resulting median probability for that object would

then be less than 50%. The object probability, however, can be much greater than 50% because while the probability of an individual pixel is not strongly indicative of ash/dust, the occurrence of a spatially coherent aggregate of pixels with a weak to moderate volcanic ash/dust multispectral signature is far less likely to be observed outside of volcanic ash and dust clouds. This concept is also akin to how humans visually identify very optically thin cirrus clouds in an otherwise sunlit blue sky. If a 1 km spatial grid were applied to the cirrus cloud area, analogous to a region of satellite pixels, and if a person's view were restricted to a given grid cell, it would be very difficult to *confidently* determine if that grid cell contained cirrus or clear sky. Conversely, when the entire collection of grid cells is viewed (analogous to a cloud object), spatial coherence makes the cirrus cloud much easier to identify, despite the fact that the amount of sunlight attenuated by the ice crystals within many of the grid cells is too small to produce the contrast required for *confident* visual identification.

4.2.1. Bayesian Method

The methodology for computing the cloud object ash/dust probability is as follows. A naïve Bayesian method is used to estimate the probability that a given *cloud object* is an ash or dust cloud. The naïve Bayesian method is formulated by assuming that the features (**F**) are independent within each class. The general naïve Bayesian approach is motivated and described in P15, so only the details required to understand the cloud object implementation are described in this paper.

Using the naïve Bayes formulation, the probability of ash or dust given an observed set of independent features [$P(C_{\text{yes}}|\mathbf{F})$] is calculated using equation (2) (the term, $P(C_{\text{yes}}|\mathbf{F})$, is also commonly referred to as the posterior probability).

$$P(C_{\text{yes}}|F) = \frac{P(C_{\text{yes}})\prod_{i=1}^{N} P(F_i|C_{\text{yes}})}{P(F)} \tag{2}$$

In equation (2), $P(C_{\text{yes}})$ is the prior probability that a given cloud object is part of an ash or dust cloud without knowledge of **F**, $P(F_i|C_{\text{yes}})$ is the estimated probability of observing a given feature (F_i) when an ash or dust cloud object is present (a total of N features are used), and $P(\mathbf{F})$ is the probability of a given set of features being observed and is computed using equation (3).

$$P(F) = P(C_{\text{yes}})\prod_{i=1}^{N} P(F_i|C_{\text{yes}}) + P(C_{\text{no}})\prod_{i=1}^{N} P(F_i|C_{\text{no}}) \tag{3}$$

In equation (3), $P(C_{\text{no}})$ is the prior probability that a given cloud object is *not* part of a volcanic ash or dust cloud [i.e., $P(C_{\text{no}}) = 1 - P(C_{\text{yes}})$] and $P(F_i|C_{\text{no}})$ is the estimated probability of observing a given feature (F_i) when an ash or dust cloud object is not present. As in P15, the prior probability of ash/dust [$P(C_{\text{yes}})$] is assumed to be 0.1%. The rationale used in selecting the prior probability is described in P15. As with the determination of the pixel-level ash/dust probability (P15), the object-based ash/dust conditional probability is often many orders of magnitude greater than the nonash/nondust conditional probability, rendering the impact of the prior probabilities minimal.

4.2.2. Cloud Object Classifiers

The class conditional probability density functions (PDFs) are empirically constructed, for each classifier (F_i), from the same extensive MODIS-based training data set described in detail in P15. The top 10 most common spectral states, by areal coverage, within a cloud object, are used as classifiers. There are many different ways to define spectral state (spectral state definition, SSD). Consistent with P15, we utilize several different multivariate definitions of spectral state. Each of the SSDs is listed in Table 1 as a function of sensor capabilities and solar illumination. The satellite sensor acronyms are defined in Table 2.

The object conditional probability for the "yes" and "no" classes are drawn from a series of empirically derived two-dimensional PDFs. The first dimension of the conditional probability PDFs corresponds to the spectral state location (SSL) or where in the SSD parameter space that portion of the cloud object resides (the multivariate SSDs shown in Table 1 are collapsed into a single vector), and the second dimension corresponds to the size of the geographic area within the object that belongs to a given SSL. The starting location of the area bins in km^2 is 1.0, 10.0, 50.0, 100.0, 500.0, 1000.0, and 5000.0. A maximum of seven SSDs can be used if the sensor has the 0.65, 3.9, 7.3, 8.5, 11, and 12 μm channels (0.65 μm is only relevant in sunlit conditions). For each SSD, the top 10 SSLs within a cloud object are used as classifiers. Thus, a maximum of 70 classifiers (F_i) can be used. If an object has less than 10 SSLs, for a given SSD, then less

Table 1. The Topmost Portion of the Table Lists the Individual Radiative Parameters Utilized to Construct Cloud Object Classifiers, Along With the Corresponding Histogram-Binning Scheme Used to Estimate the Classifier PDFs[a]

Parameter [Parameter ID]	Number of Histogram Bins	Starting Boundaries of Histogram Bins
ε_{tot}(11 μm) [1]	4	0.00, 0.03, 0.10, 0.30
β_{tot}(12 μm, 11 μm) [2]	7	0.00, 0.70, 0.80, 0.90, 0.95, 0.98, 1.00
β_{opaque}(12 μm, 11 μm) [3]	7	0.00, 0.50, 0.90, 1.00, 1.10, 1.20, 1.30
β_{tot}(8.5 μm, 11 μm) [4]	5	0.00, 0.90, 1.10, 1.30, 1.80
β_{opaque}(8.5 μm, 11 μm) [5]	5	0.00, 0.90, 1.10, 1.30, 1.80
β_{tot}(7.3 μm, 11 μm) [6]	5	0.00, 1.00, 1.50, 2.00, 3.00
ρ(3.9 μm, 0.65 μm) [7]	5	0.00, 0.20, 0.50, 0.80, 1.00
ε_p(3.9 μm) [8]	5	0.00, 0.90, 1.00, 1.20, 1.40
BTD(11–12 μm) [9]	7	−20.00, −2.00, −1.00, −0.75, −0.50, −0.25, 0.00 K
BT_{sdev}(11 μm) [10]	11	0.0, 0.25, 0.50, 0.75, 1.0, 2.0, 3.0, 4.0, 5.0, 6.0, 7.0 K
ref_{sdev}(0.65 μm) [11]	11	0.0, 1.0, 2.0, 3.0, 4.0, 5.0, 6.0, 7.0, 8.0, 9.0, 10.0%
Indicators of Spectral State	**Relevant Sensors**	**Conditions**
[1] × [2] × [7] [1] × [3] × [7] [1] × [9] × [7] [1] × [11]	AVHRR[b] COMS-MI GOES Imager[c] GOES-R ABI Himawari-8/9 AHI MODIS MTSAT Imager MSG SEVIRI MTG FCI VIIRS	Only applied when at least 25% of the cloud object pixels are outside of sunglint and have a solar zenith angle that is less than 85°
[1] × [2] × [8] [1] × [3] × [8] [1] × [9] × [8] [1] × [10]	AVHRR[b] COMS-MI GOES Imager[c] GOES-R ABI Himawari-8/9 AHI MODIS MTSAT Imager MSG SEVIRI MTG FCI VIIRS	Only applied when at least 25% of the cloud object pixels have a solar zenith angle greater than 90° while not under the influence of stray light
[1] × [2] × [4] [1] × [3] × [5]	GOES-R ABI Himawari-8/9 AHI MODIS MSG SEVIRI MTG FCI VIIRS	Applied at all times
[1] × [2] × [6]	GOES-R ABI Himawari-8/9 AHI MODIS MSG SEVIRI MTG FCI	Applied at all times
[1] × [2] [1] × [3] [1] × [9] [1] × [10]	AVHRR[b] COMS-MI GOES Imager[c] GOES-R ABI Himawari-8/9 AHI MODIS MTSAT Imager MSG SEVIRI MTG FCI VIIRS	Only applied when less than 25% of the cloud object pixels fail to meet the daytime or nighttime requirements

[a]The multivariate classifier variables (using the radiative parameter IDs shown in the top part of the table) are listed in the second part of the table as a function of satellite sensor and the conditions required for utilization. Sunglint is assumed to be present over water surfaces if the glint angle is less than 40°. Stray light is assumed to be present if the solar zenith angle exceeds 90° and the measured 0.65 μm counts is greater than a sensor-dependent threshold. Please see Table 2 for a list of sensor acronyms.

[b]The analogue to the 3.9 μm band on advanced very high resolution radiometer (AVHRR) (the 3.75 μm band) is currently not available on the MetOp-A and MetOp-B spacecraft during daytime operations.

[c]The 12 μm channel is only available on the GOES 8–11 spacecraft.

Table 2. The Satellite Imaging Radiometers of Greatest Relevance to the Ash/Dust Detection Algorithm Described in This Paper Is Listed Below[a]

Sensor Acronym	Acronym Meaning
AVHRR	Advanced very high resolution radiometer
COMS MI	Communication, Ocean, and Meteorological Satellite (COMS) Meteorological Imager (MI)
GOES Imager	Geostationary Operational Environmental Satellite (GOES) Imager
GOES-R ABI[b]	Next Generation Geostationary Operational Environmental Satellite (GOES-R) Advanced Baseline Imager (ABI)
Himawari-8/9 AHI[b]	Himawari-8/9 Advanced Himawari Imager (AHI)
MODIS	Moderate Resolution Imaging Spectroradiometer
MTSAT Imager	Multifunctional Transport Satellites (MTSAT) Imager
MSG SEVIRI	Meteosat Second Generation (MSG) Spinning Enhanced Visible and Infrared Imager
MTG FCI[b]	Meteosat Third Generation (MTG) Flexible Combined Imager (FCI)
VIIRS	Visible Infrared Imaging Radiometer Suite

[a]Each sensor may be present on multiple spacecraft with different orbital parameters.
[b]Capability will be launched and deployed in 2014 or later.

than 10 SSLs are used (the cloud object area corresponding to a given SSL must be greater than 1 km^2). In addition, when the SSL is defined by a ε_{tot}(11 μm) that is less than 0.03, the conditional probability for the yes and no classes is set to 1.0 to avoid using pixels that exhibit very little deviation from clear-sky conditions at 11 μm in the object selection process.

4.2.3. Cloud Object Probability Illustration

The cloud object probability is shown in Figure 1f. Several cloud objects within the ROI have a very large probability (~100%), while all of the cloud objects outside of the ROI generally have much lower probabilities. The 10 most common (by area) SSLs within the cloud object (labeled with a "1" in Figure 1f) are shown in Figure 2 using six different SSDs. Note that cloud object 1 is located inside the ROI. Each bar in each panel of Figure 2 represents a classifier in the cloud object-based Bayesian method. The magnitude of each bar depicts the area within the cloud object that falls within a given SSL (the area is shown on the *y* axis on the left). The bar color represents the ratio of the ash/dust conditional probability to the nonash/nondust conditional probability, where the cyan to red color range indicates that the ash/dust conditional probability is greater than or equal to the nonash/nondust conditional probability. The specific parameters that define the SSL are also labeled on each bar. The box-and-whisker plot of the pixel ash/dust probability distribution within a given SSL in the cloud object is overlaid in black and referenced to the *y* axis on the right of each panel. Figure 2 indicates that even SSLs that are generally associated with pixel-level ash/dust probabilities that are less than 50% often have conditional probabilities that favor ash/dust (or vice versa). It is no surprise that the posterior cloud object probability is ~100%, as the posterior cloud object probability computed using a single SSD (or single panel in Figure 2) is also quite large (>95% in most cases). This analysis was repeated for the cloud object that resides outside of the ROI in Figure 1f and is labeled with a "2" (see Figure 3). Unlike object 1, less than 10 SSLs were identified in object 2 and the observed features do not favor volcanic ash/dust, regardless of the method used to define spectral state. The posterior cloud object probability is close to zero, as one might expect for a meteorological cloud feature. The analysis shown in Figures 1–3 indicates that the cloud object implementation of the Bayesian method produces reasonable results and complements the pixel-level probability information.

4.2.4. Spectral Robustness

Another method for quantitatively rating the overall spectral robustness of a given cloud object, with respect to volcanic ash and dust, is to determine how many pixels in the object exhibit a multispectral signature that is very rarely observed outside of volcanic ash and dust clouds. Although the pixel-level Bayesian model was shown to be quite skillful, a pixel-level ash/dust probability close to 100% does not always correspond to volcanic ash or dust, primarily because the naïve Bayesian method cannot perfectly account for land surface emissivity effects, errors in the computation of clear-sky radiances, and measurement artifacts. Thus, seven additional metrics are used along with the pixel-level ash/dust probability to rate the spectral robustness of a given pixel. The additional metrics utilized are the following: the 11 μm clear-sky brightness temperature [BT_{clr}(11 μm)], ε_{tot}(11 μm), BT_{sdev}(11 μm), BTD(11–12 μm), BTD(8.5–11 μm), β_{tot} (7.3 μm, 11 μm), and β_{tot}(8.5 μm, 11 μm). These metrics were chosen because the values of many different combinations of these variables are rarely observed outside of volcanic ash and dust clouds, including in

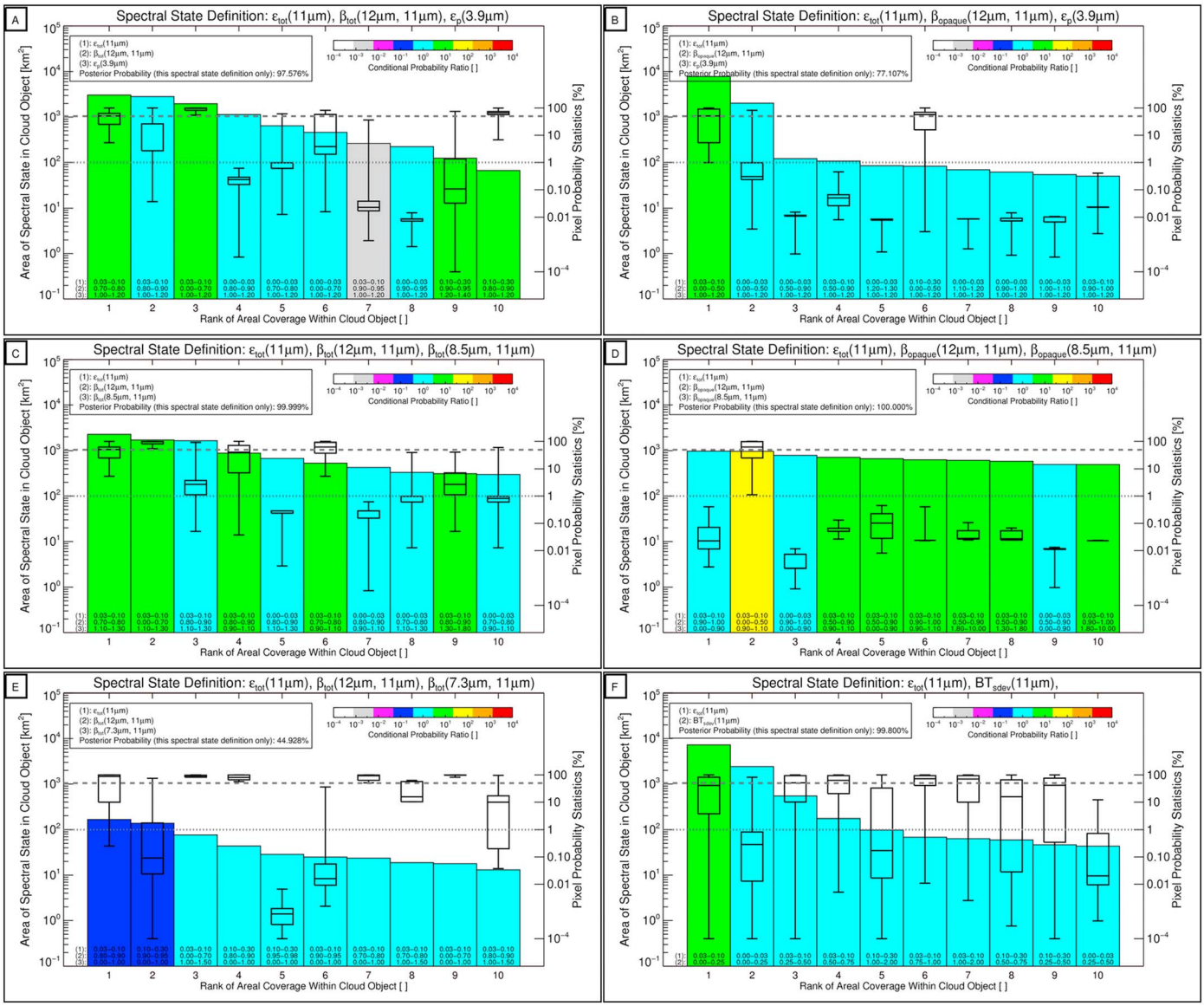

Figure 2. The procedure used to determine the probability that a cloud object is part of a volcanic ash or dust cloud is illustrated. Each panel represents a different method for quantifying the spectral states within a cloud object (see panel titles for spectral state definition). The 10 most common spectral states (for a given definition) within the cloud object labeled 1 in Figure 1f are denoted by the colored bars. The magnitude of the bar is representative of the area within the cloud object that exhibits a given spectral state (the area is shown on the *y* axis on the left). The bar color represents the ratio of the ash/dust conditional probability to the nonash/nondust conditional probability, where the cyan to red color range indicates that the ash/dust conditional probability is greater than or equal to the nonash/nondust conditional probability. The specific parameters that define each spectral state are also labeled at the bottom of each bar. Finally, the box-and-whisker plot of the pixel ash/dust probability distribution within a given spectral state in the cloud object is overlaid in black and referenced to the *y* axis on the right of each panel. The dotted and dashed horizontal gray lines indicate a pixel probability value of 1% and 50%, respectively.

association with measurement artifacts such as noise and band-to-band coregistration errors and errors in the clear-sky radiative transfer. In addition, only a small number of histogram bins are required, for each metric, to keep track of values that are potentially associated with a robust ash/dust spectral signature, making it practical to construct an eight-dimensional histogram. The histogram bins are defined in Table 3. The MODIS-based training data set described in P15 was used to construct an eight-dimensional histogram from volcanic ash/dust pixels and separately from all other pixels in the training data set. The training database for the ash/dust class consists of about 6.5 million volcanic ash pixels and 3.7 million desert dust pixels. A total of about 2.5 billion nonvolcanic ash/dust pixels, drawn from 2401 different 5 min MODIS granules, were used to construct the training database for the nonash/nondust class. To avoid

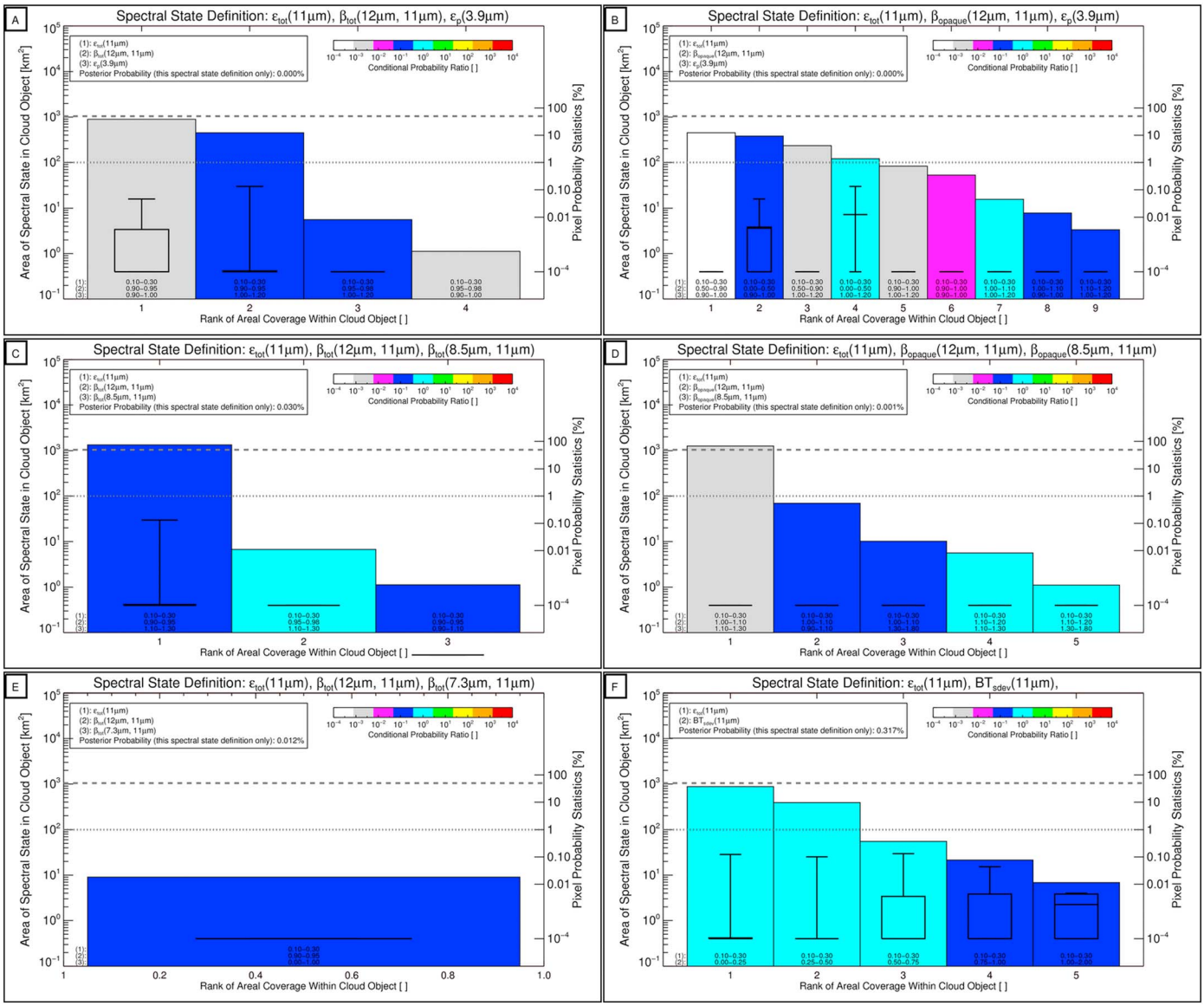

Figure 3. Same as Figure 2 except for the cloud object labeled with a 2 in Figure 1f. Less than 10 spectral states were found in object 2, regardless of the mechanism for defining spectral state.

Table 3. The Radiative Parameters That Define an Eight-Element State Vector, Where Each Element Is Discretized Using the Associated Histogram-Binning Scheme, Are Shown

Parameter [Dimension Index]	Number of Histogram Bins	Starting Boundaries of Histogram Bins
BT_{clr}(11 μm) [1]	4	160, 250, 270, 290 (K)
ε_{tot}(11 μm) [2]	8	0.00, 0.05, 0.08, 0.10, 0.20, 0.40, 0.60, 0.80
BT_{sdev}(11 μm) [3]	6	0.00, 0.50, 1.00, 2.00, 5.00, 10.00 (K)
BTD(11–12 μm) [4]	14	−50.00, −25.00, −2.50, −2.00, −1.50, −1.00, −0.75, −0.50, −0.25, −0.10, 0.0, 0.25, 0.50, 1.00 (K)
BTD(8.5–12 μm) [5]	11	−50.00, −25.00, −1.50, −1.25, −1.00, −0.75, −0.50, −0.25, 0.00, 0.25, 0.50 (K)
β_{tot}(7.3 μm, 11 μm) [6]	5	0.00, 0.10, 1.50, 1.80, 2.00
β_{tot}(8.5 μm, 11 μm) [7]	8	0.00, 0.10, 0.80, 0.90, 1.00, 1.50, 1.80, 2.00
$P(C_{yes}\|F)$ [8]	10	0, 10, 50, 90, 99, 99.9, 99.99, 99.999, 99.9999, 99.999999 (%)

cross contamination, the nonash/nondust training pixels were taken from MODIS granules that were independent of those used to construct the ash/dust component of the training. Regions of ash and dust were inferred through manual analysis of multispectral imagery. Even though the training data set is very large, the eight-dimensional histogram is likely undersampled, which is one of the reasons that a naïve Bayesian approach, with lower dimensional classification features, is utilized to assign pixel and object probabilities. The eight-dimensional histograms, however, are only utilized to identify pixels that have a discretized (i.e., individual values are assigned to a histogram bin) eight-element state vector that was observed inside of ash and/or dust clouds in the training data but otherwise were rarely observed in the training data. Several satellite sensors lack the spectral channels required to compute the BTD(8.5–11 μm), β_{tot}(7.3 μm, 11 μm), and β_{tot}(8.5 μm, 11 μm) parameters (see Tables 1 and 2). When the 7.3 and/or 8.5 μm channels are not available, all observations are assigned to the first histogram bin of the parameter(s) that cannot be computed.

The eight-dimensional histograms are used to derive a spectral robustness rating for each histogram bin that ranges from 0 (not robust) to 4 (very robust). The robustness rating was derived separately for desert surfaces since multispectral surface emissivity signatures over desert can closely resemble volcanic ash and dust clouds and errors in the clear-sky radiative transfer calculations are generally greatest over desert. For nondesert surfaces, the ash/dust histogram contains about 10 million observations and the nonash/nondust histogram contains 2.3 billion observations. For desert surfaces, the ash/dust histogram contains about 100,000 observations and the nonash/nondust histogram contains 4.7 million observations. The discrepancy in sampling was considered when choosing guidelines that map each histogram bin into a robustness rating. For a given histogram bin, the number of ash/dust observations (N_{ash}), the number of nonash/nondust observations (N_{other}), and the number of nonash/nondust observations normalized by the total number of observations (ash/dust + nonash/nondust) in that bin (R_{other}) are used to assign the robustness rating (RR). Each bin is assigned the highest robustness rating possible using the following rules.

$$RR = \begin{cases} 4, & N_{ash} > 5 \text{ and } N_{other} = 0 \\ & N_{ash} > 0 \text{ and } N_{other} < 0 \text{ or} \\ & N_{ash} > 1 \text{ and } N_{other} < 2 \text{ or} \\ 3, & N_{ash} > 5 \text{ and } N_{other} < 50 \text{ and } R_{other} < 0.01 \text{ or} \\ & N_{ash} > 5 \text{ and } N_{other} < 10 \text{ and } R_{other} < 0.10 \\ & N_{ash} > 0 \text{ and } N_{other} < 10 \text{ or} \\ 2, & N_{ash} > 5 \text{ and } 50 \leq N_{other} < 100 \text{ and } R_{other} < 0.01 \text{ or} \\ & N_{ash} > 5 \text{ and } 10 \leq N_{other} < 50 \text{ and } R_{other} < 0.10 \\ & N_{ash} > 0 \text{ and } N_{other} < 100 \text{ or} \\ 1, & N_{ash} > 5 \text{ and } N_{other} < 500 \text{ and } R_{other} < 0.50 \\ 0, & \text{otherwise} \end{cases} \tag{4}$$

Each pixel in a given cloud object is assigned a robustness rating using the eight-dimensional robustness look-up table generated from the data used to train the Bayesian methods. The total number of pixels in each robustness category can then be computed for each cloud object. Returning to the nighttime Cleveland volcanic ash example, the fraction of each cloud object that achieves robustness rating 2 through 4 is shown in Figures 1g–1i, with robustness rating decreasing from left to right. The robustness counter is incremented for a given rating (0–4) if a rating at or above that level is achieved. For instance, a robustness rating of 3 results in the object counter for rating values 0 to 3 being incremented. In Figures 1g–1i the robustness fraction is only displayed if it is greater than 0%; otherwise, the 11 μm brightness temperature is displayed. Only two cloud objects were found to include pixels with a robustness rating of 3 or greater, and both objects were located inside the ROI. Five cloud objects, all within the ROI, were found to contain pixels with a robustness rating of 2 or greater. Not surprisingly, the two objects with level 3 or greater robust pixels correspond to regions of the ash cloud that are readily

apparent in the false color and split window images. The cloud objects that contain pixels with a robustness rating no higher than 2 have a much less impressive visual appearance in the multispectral imagery. Thus, the robustness rating of all of the objects is qualitatively consistent with how a human expert would rate the strength of the volcanic ash spectral signature at various locations in the cloud. Finally, the robustness rating procedure allows for a greater degree of sensor-dependent customization without the need of retraining the Bayesian model. Thus, the SECO method can be effectively applied to new sensors immediately, simply by adjusting the robustness rating look-up table until the false alarm rate is as low as expected.

4.3. Identifying Potential Clear-Sky Objects

As discussed in P15, errors in the clear-sky radiative transfer calculations can be large at times, especially over land surfaces. Thus, some "cloud" objects may actually be composed entirely of clear-sky pixels when the clear-sky radiances are significantly overestimated. If the spectral variability of the surface emissivity is similar to volcanic ash and dust, the clear-sky object can potentially be misclassified as volcanic ash/dust. A spatial analysis technique is used to address this issue. The difference between the clear-sky 11 μm BT and the observed 11 μm BT, referred to as the clear-sky bias or BT_{bias}, is assessed at various locations inside and outside of cloud objects. More specifically, the mean "in object" and "environmental" BT_{bias} is computed for each object. The in object BT_{bias} (BT_{bias_obj}) is computed from object pixels that have a pixel-level ash/dust probability smaller than 10%. The environmental BT_{bias} (BT_{bias_env}) is computed from nearby (e.g., within 12 pixels of the edge of the object of interest) out of object pixels that have an ash/dust probability less than 0.10 and are likely to be free of meteorological cloud. Meteorological cloud cover is assessed using the metrics described in *Heidinger et al.* [2012]. Each cloud object is assigned a cloud flag (CF) ranging from 0 (confidently clear) to 3 (confidently cloudy) depending on the BT_{bias_obj} and the difference between BT_{bias_obj} and BT_{bias_env} (BTD_{bias_diff}). The binary cloud object classifier utilizes the cloud flag. The guidelines for assigning the cloud flag are provided below.

$$\mathrm{cf} = \begin{cases} 3 & \mathrm{BTbias_obj} > 18\ \mathrm{K\ or\ BTbias_{diff}} > 6\ \mathrm{K} \\ 2 & 4 < \mathrm{BTbias_{diff}} \leq 6 \\ 1 & 2 < \mathrm{BTbias_{diff}} \leq 4 \\ 0 & \mathrm{BTbias_{diff}} \leq 2 \end{cases}$$

4.4. Binary Classification of Cloud Objects

Using the various cloud object statistics described earlier, a simple binary cloud object classifier was developed. Cloud objects can be classified as volcanic ash/dust or not. If a cloud object is classified as volcanic ash/dust, all pixels that compose the cloud object are classified as volcanic ash/dust. The basic binary classifier, also referred to as the cloud object selection procedure, is a function of the cloud object size (in pixels), the median ash/dust pixel probability, the cloud object referenced probability of ash/dust, the cloud confidence flag, and the robustness rating metrics. Many different threshold combinations are utilized based on heuristic analysis of the training data set and subsequent global real-time testing of the SECO algorithm. All of the threshold combinations utilized in the cloud object selection process are listed in Table 4. Each row in the table represents a set of cloud object selection criteria (each row of Table 4 is equivalent to a logical "OR" operator). During the cloud object selection process, the "greater than" operator is applied to all criteria except the maximum cloud object size and cloud confidence. The "less than or equal to" operator is applied to the maximum cloud object size, and the "greater than or equal to" operator is applied to the cloud confidence flag. If any single set of selection criteria is met, the cloud object is selected (all pixels within that object are classified as ash/dust).

5. Case Studies

An initial assessment of the complete SECO volcanic ash/dust detection algorithm is conducted by analyzing four ash/dust cases captured by MODIS. The same four cases shown in P15 are utilized. Each of the four cases (two volcanic ash and two dust) is independent of the classifier training data, and the ash/dust probability is assessed within the context of human expert-estimated horizontal cloud boundaries and the traditional split window technique for detecting volcanic ash and dust. As in P15, results from the SECO algorithm were

Table 4. Each Row in the Table Represents a Set of Cloud Object Selection Criteria[a]

Min Size (#pix)	Max Size (#pix)	Median Prob %	Object Prob %	Cloud Flag (CF)	RR4 Ct	RR4 Frac	RR3 Ct	RR3 Frac	RR2 Ct	RR2 Frac	RR1 Ct	RR1 Frac
25	∞	0	80	2	4	0.0000	14	0.0000	0	0.0000	0	0.0000
25	∞	80	0	2	4	0.0000	14	0.0000	0	0.0000	0	0.0000
250	∞	0	80	2	0	0.0100	0	0.0000	0	0.0000	0	0.0000
250	∞	80	0	2	0	0.0100	0	0.0000	0	0.0000	0	0.0000
100	∞	0	80	2	0	0.0050	0	0.0100	0	0.0000	0	0.0000
100	∞	80	0	2	0	0.0050	0	0.0100	0	0.0000	0	0.0000
5000	∞	20	99	2	−1	−0.10	−1	−0.10	10	0.0000	3000	0.0000
250	∞	0	80	0	100	0.0000	0	0.0000	0	0.0000	0	0.0000
250	∞	80	0	0	100	0.0000	0	0.0000	0	0.0000	0	0.0000
500	∞	0	80	0	0	0.0000	500	0.0000	0	0.0000	0	0.0000
500	∞	80	0	0	0	0.0000	500	0.0000	0	0.0000	0	0.0000
100	1000	80	80	2	−1	−0.10	0	0.0100	0	0.0133	0	0.0500
250	500	0	80	2	0	0.0000	0	0.0055	0	0.0133	0	0.0500
250	500	80	0	2	0	0.0000	0	0.0055	0	0.0133	0	0.0500
100	250	0	80	2	0	0.0050	0	0.0100	0	0.0000	0	0.0000
100	250	80	0	2	0	0.0050	0	0.0100	0	0.0000	0	0.0000
25	250	0	80	2	0	0.0000	0	0.0000	0	0.0133	0	0.0500
25	250	80	0	2	0	0.0000	0	0.0000	0	0.0133	0	0.0500
15	25	80	80	2	4	0.0000	14	0.0000	0	0.0000	0	0.0000
10	25	80	80	2	0	0.0000	0	0.0000	0	0.0133	0	0.0500
				V50								
10	25	80	0	3	−1	−0.10	−1	−0.10	0	0.2500	0	0.5000
10	25	80	80	3	−1	−0.10	−1	−0.10	0	0.1000	0	0.5000
0	10	80	0	3	−1	−0.10	−1	−0.10	0	0.2500	0	0.5000
0	10	80	80	3	−1	−0.10	−1	−0.10	0	0.1000	0	0.5000
				V10								
10	25	0	80	3	0	0.0000	0	0.0000	0	0.0133	0	0.0500
10	25	80	0	3	0	0.0000	0	0.0000	0	0.0133	0	0.0500
				V5								
0	10	80	0	3	0	0.0000	0	0.0000	0	0.0133	0	0.0500
0	10	0	80	3	0	0.0000	0	0.0000	0	0.0133	0	0.0500

[a]During the cloud object selection process the greater than operator is applied to all criteria except "max size" and "cloud flag." The less than or equal to operator is applied to max size, and the greater than or equal to operator is applied to cloud flag. If any single set of selection criteria is met, the cloud object is selected. The center of the cloud object must be within 50/10/5 km of a volcano in order to use the criteria listed below the V50/V10/V5 headers. #pix: number of pixels, Prob: ash/dust probability, RR: robustness rating, Ct: count, and Frac: fraction.

generated using four different spectral channel combinations that are commonly available on operational and research satellite radiometers. (1) 0.65 (daytime only), 3.9, 7.3, 8.5, 11, and 12 μm (SC1, SC = spectral combination); (2) 0.65 (daytime only), 3.9, 8.5, 11, and 12 μm (SC2); (3) 0.65 (daytime only), 3.9, 11, and 12 μm (SC3); and (4) 11 and 12 μm (SC4).

The results from the manual analysis first presented in P15 are once again utilized. As described in P15, the goal of the manual analysis of the ash/dust cloud boundaries was to define a ROI that contains the portion of the ash/dust cloud that can be manually identified in multispectral imagery, either directly or through spatial deduction. All conclusions drawn from the comparison to the manually determined ROI are derived from relative relationships. As such, small perturbations to the ROI do not impact the results as long as ash or dust pixels that exhibit a robust spectral signature (i.e., are obvious in the imagery) are not left out of the ROI.

5.1. Volcanic Ash From Mount Cleveland (Nighttime)

SECO algorithm results from each spectral channel combination are shown in Figure 4 for the same nighttime Cleveland volcanic ash scene discussed earlier. The binary classifier (described in section 4.4) results are displayed using the pixel-level ash/dust probability and the 11 μm brightness temperature imagery. Where the binary classifier indicates that volcanic ash or dust is present, the pixel-level probability is displayed; otherwise, the 11 μm brightness temperature is displayed. The pixel-level probability is displayed to demonstrate how the object-based selection methodology includes pixels with a strong ash/dust spectral

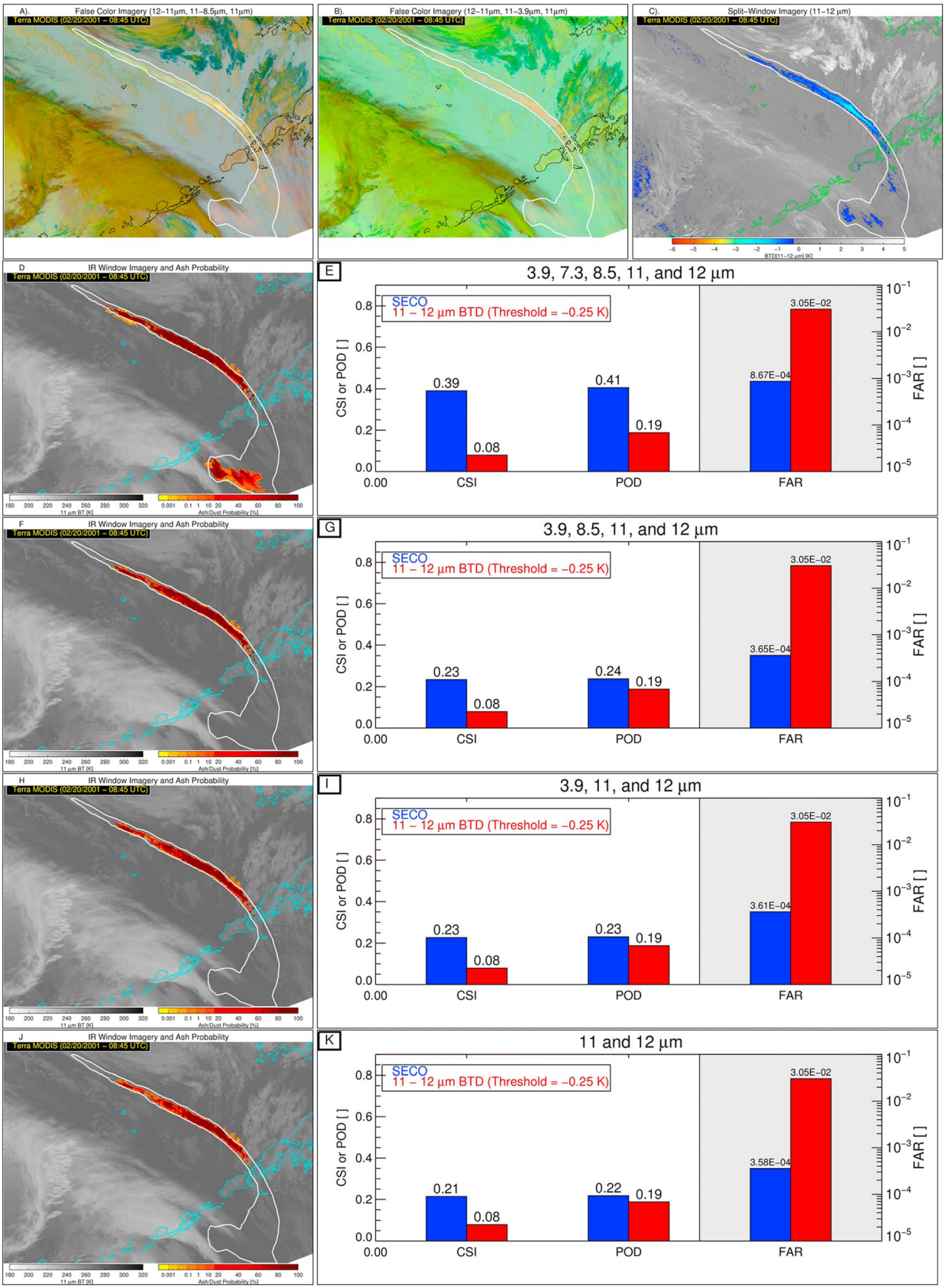
A). False Color Imagery (12–11μm, 11–8.5μm, 11μm)
B). False Color Imagery (12–11μm, 11–3.9μm, 11μm)
C). Split-Window Imagery (11–12 μm)
Terra MODIS (02/20/2001 – 08:45 UTC)
D IR Window Imagery and Ash Probability
E 3.9, 7.3, 8.5, 11, and 12 μm
F IR Window Imagery and Ash Probability
G 3.9, 8.5, 11, and 12 μm
H IR Window Imagery and Ash Probability
I 3.9, 11, and 12 μm
J IR Window Imagery and Ash Probability
K 11 and 12 μm
SECO
11 – 12 μm BTD (Threshold = –0.25 K)
CSI or POD [ ]
FAR [ ]
CSI
POD
FAR
0.39
0.08
0.41
0.19
8.67E–04
3.05E–02
0.23
0.08
0.24
0.19
3.65E–04
3.05E–02
0.23
0.08
0.23
0.19
3.61E–04
3.05E–02
0.21
0.08
0.22
0.19
3.58E–04
3.05E–02

Figure 4

signal (high probabilities) as well as pixels with a weaker ash/dust spectral signature (low probabilities). As in P15, the critical success index (CSI), which is defined as the number of hits divided by the sum of hits, false alarms, and misses, is utilized to quantify the skill of the SECO algorithm *relative* to the manual analysis. The CSI does not take correct negatives into account, so it is an effective metric when the event of interest is observed far less often than the nonevents and the tolerance for false alarms is low (volcanic ash false alarms are particularly undesirable). Also, given the relative nature of the case study analysis (e.g., comparing SECO results from different channel combinations to traditional split window results), the exact choice of skill statistic is not overly important. The split window results were derived using the traditional threshold method. The BTD(11–12 μm) threshold, however, was selected such that it maximized the CSI for each 5 min MODIS granule by stepping through the range of BTD values in 0.01 K increments and identifying the BTD threshold that maximizes the CSI. Thus, the *best possible*, case-specific, split window results are shown (which will not necessarily be known in real time). The probability of detection (POD) and false alarm rate (FAR) are also computed. While all of the statistics are relative to the 5 min MODIS granule, only a subset of the granule is imaged for the sake of clarity. The MODIS overpass shown in Figure 4 occurred about 18.25 h after the start of the eruption of Mount Cleveland. As a result, the volcanic ash cloud has been advected northeastward of the volcano by the atmospheric winds and the entire ash cloud is highly semitransparent to infrared radiation due to dispersion and fallout processes. In fact, portions of the southern part of cloud can only be confidently identified in multispectral false color imagery through spatial deduction.

Figure 4 shows that the SECO algorithm is much more skilled than the split window approach, which was intentionally optimized for this particular scene, regardless of the spectral channel combination. In this scene the CSI of the SECO algorithm is 0.39, 0.23, 0.23, and 0.21 for the SC1, SC2, SC3, and SC4 implementations, respectively. The split window approach only achieves a CSI of 0.08, making the CSI of the SC1 implementation of the SECO algorithm almost 5 times greater than the split window approach. Even when the SECO algorithm utilizes the exact same spectral channels as the split window approach (the SC4 implementation), the skill of the SECO algorithm is much greater, which underscores the value of using β ratios in lieu of BTDs and cloud objects in lieu of individual pixels. Unlike the split window approach, all SECO algorithm ash/dust detections occur within the ROI or just barely outside of the ROI (this is true for the entire 5 min MODIS granule) and the 11–12 μm BTD need not be negative in order to detect volcanic ash. The POD of the SECO method is greater than the split window method, regardless of the channel combination utilized. Further, the FAR of the SECO method is nearly 2 orders of magnitude less than the split window technique and the proximity of the SECO "false alarms" to the edge of the manually analyzed cloud casts some doubt as to their true nature.

As expected, the skill of the SECO approach decreases when spectral channels are removed. In fact, the portion of the ash cloud south of Alaska's Aleutian Islands is only partially detected using the SC1 implementation; only the SC1 implementation results in the object labeled 1 in Figure 1f having a sufficient number of spectrally robust pixels to be selected. However, as Figure 5 shows, even the two-channel SC4 implementation results in many cloud objects within the ROI. While many of those objects lack the properties required for selection by the basic cloud object selection procedure, the mere presence of those objects within the ROI means that the prospect of improving the POD of the SECO algorithm through improvements in the cloud object selection procedure is good. For instance, future versions of the SECO cloud object selection procedure will include the ability to utilize the results from previous images, regardless of sensor.

Figure 4. The results of the SECO volcanic ash and dust detection algorithm are shown for a nighttime Terra MODIS image of volcanic ash erupted from Mount Cleveland (Alaska) on 20 February 2001 at 08:45 UTC. (a) 12–11 μm, 11–8.5 μm, and 11 μm false color image. (b) 12–11 μm, 11–3.9 μm, and 11 μm false color image. (c) Image of BTD(11–12 μm). (d) Ash/dust pixel probability image for 0.65, 3.9, 7.3, 8.5, 11, and 12 μm channel combinations. (e) The SECO algorithm skill (blue bars) measured against manual analysis of multispectral imagery is expressed as the critical success index (CSI), probability of detection (POD), and false alarm rate (FAR). The skill of the traditional split window method using the BTD(11–12 μm) threshold that produces the greatest CSI for this particular scene is also shown (red bars). (f–k) Analogous to Figures 4d and 4e except for the 3.9, 8.5, 11, 12 μm, 3.9, 11, 12 μm, and 11, 12 μm channel combinations, respectively. The outer bounds of the manually defined ash/dust cloud are overlaid on each georeferenced image.

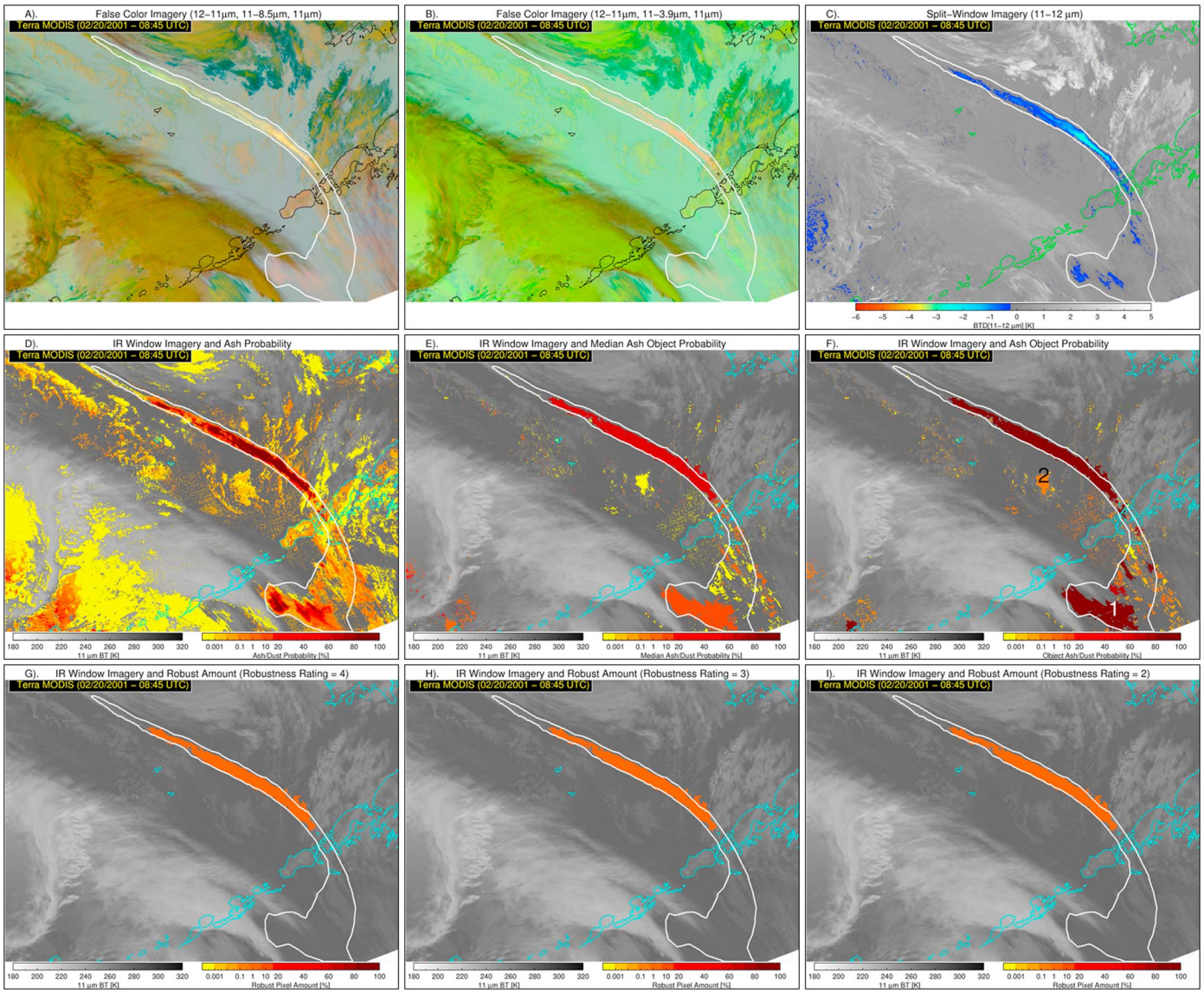

Figure 5. Same as Figure 1 except only the 11 and 12 μm channels were used to generate these results.

5.2. Volcanic Ash From Mount Cleveland (Daytime)

As in P15, the *Terra* MODIS overpass of the Cleveland ash cloud that occurred about 9.5 h prior to nighttime Cleveland example was also analyzed (see Figure 6). The exact starting date and time of the Terra MODIS granule is 19 February 2001 at 23:10 UTC, and the overpass occurred under sunlit conditions and at a time when the Cleveland plume was less dispersed. SECO algorithm results (described in section 4.4) from each spectral channel combination are shown in Figure 6. As in the previous example, the SECO algorithm is much more skilled than the split window approach, which was intentionally optimized for this particular scene, regardless of the spectral channel combination. In this scene the CSI of the SECO algorithm is 0.63, 0.61, 0.59, and 0.58 for the SC1, SC2, SC3, and SC4 implementations, respectively. The split window approach achieves a CSI of 0.13, making the CSI of the SC1 implementation of the SECO algorithm more than 5 times greater than the split window approach. Even when the SECO algorithm utilizes the exact same spectral channels as the split window approach (the SC4 implementation), the skill of the SECO algorithm is much greater, which again underscores the value of using β ratios in lieu of BTDs and cloud objects in lieu of individual pixels. All SECO false alarms once again reside along the edge of the manually

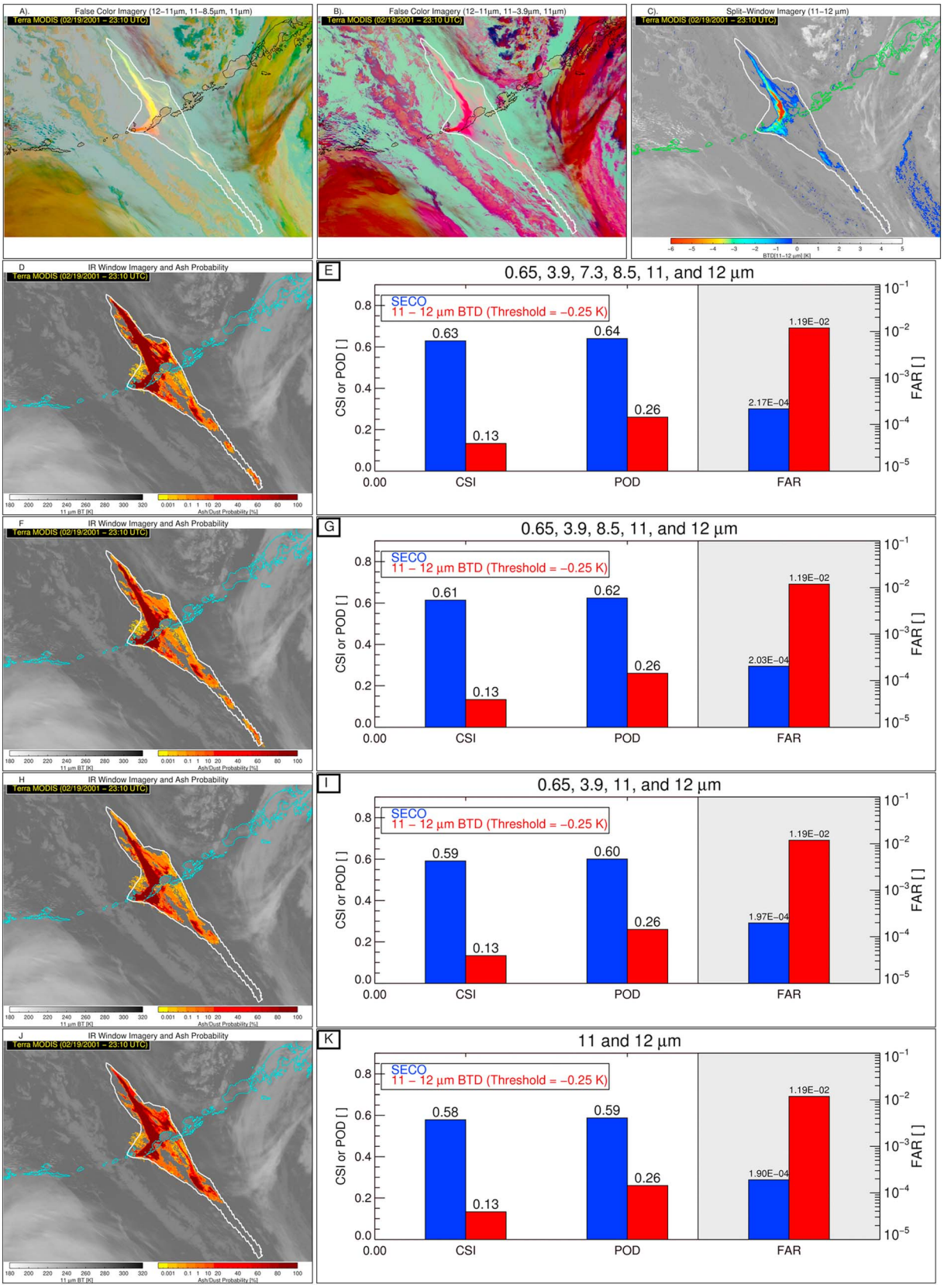

Figure 6. Same as Figure 4 except the results are shown for a sunlit (the 0.65 μm channel is used) Terra MODIS image containing regions of ash erupted by Mount Cleveland (Alaska). The MODIS image was taken on 19 February 2001 at 23:10.

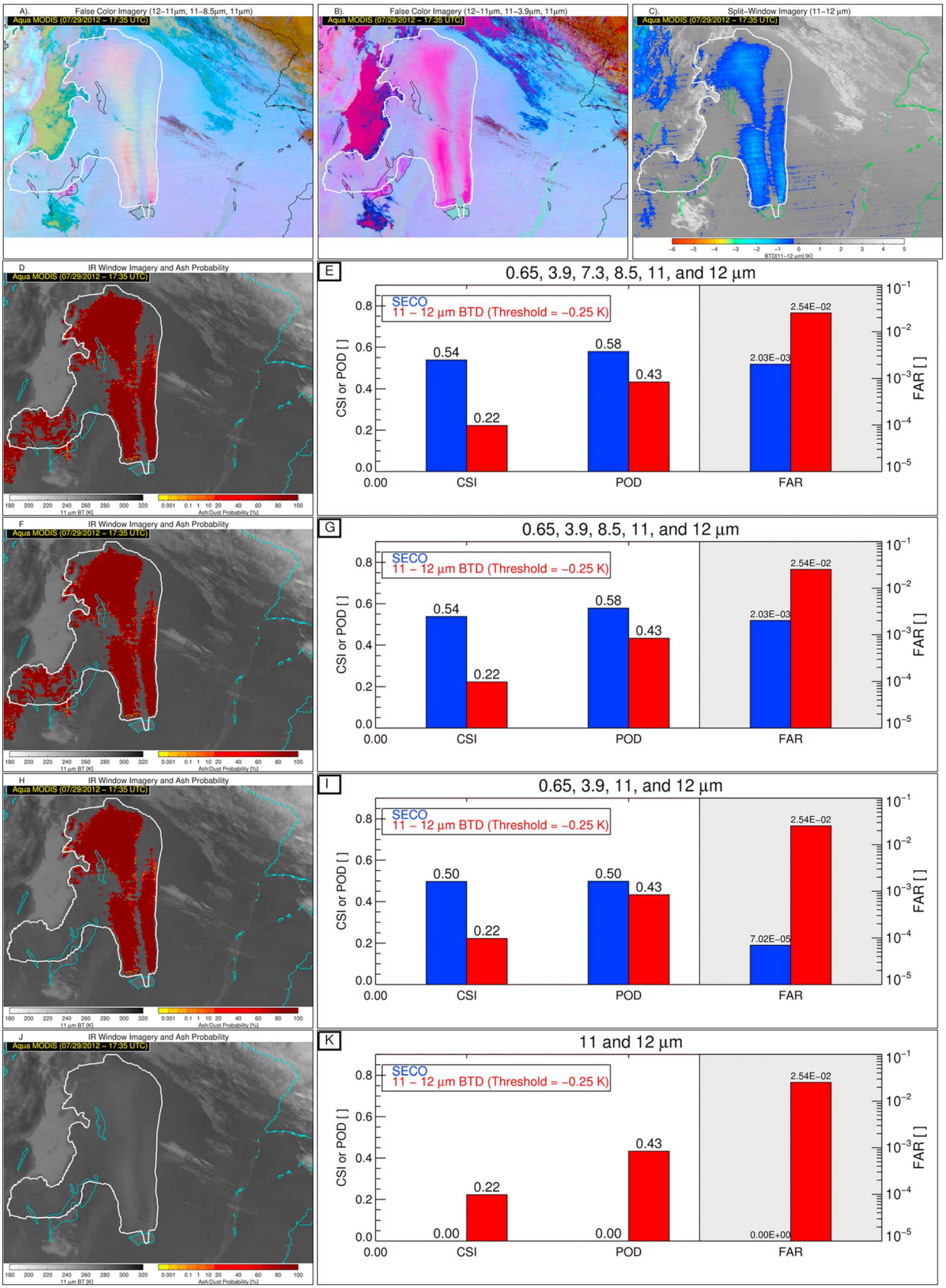

Figure 7. Same as Figure 4 except the results are shown for a sunlit (the 0.65 μm channel is used) Aqua MODIS image over central Argentina on 29 July 2012 at 17:35.

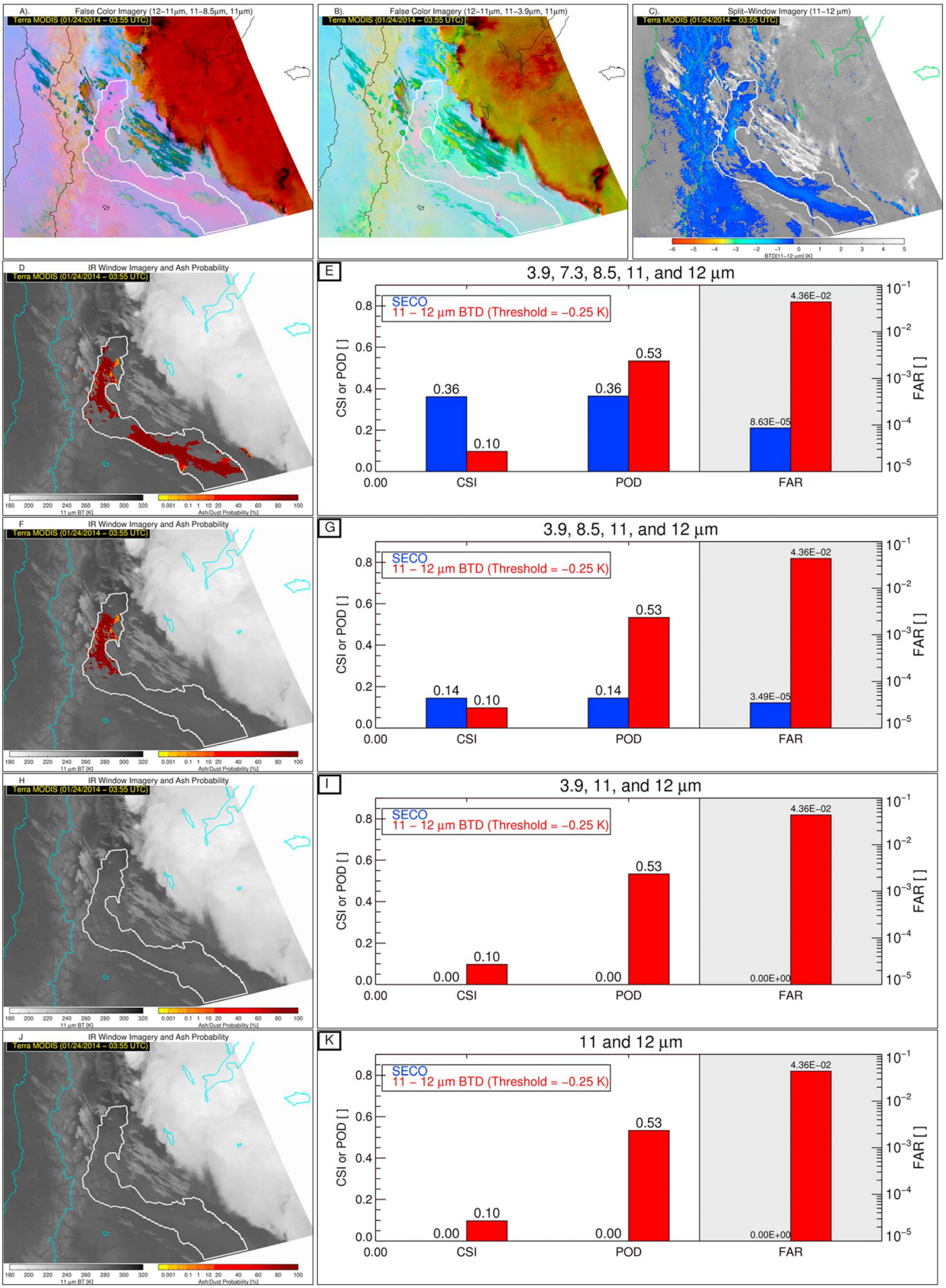

Figure 8. Same as Figure 4 except the results are shown for a nighttime Terra MODIS image over western Argentina on 24 January 2014 at 03:55.

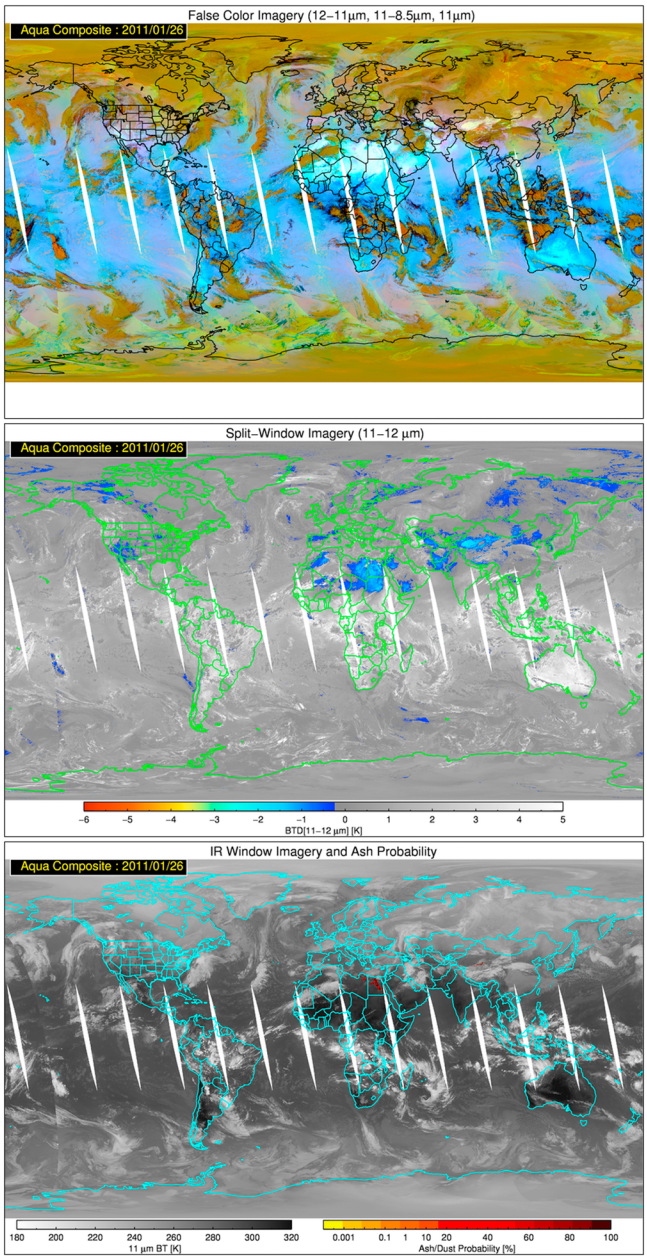

Figure 9. False color imagery constructed from the (top row) 12–11, 11–8.5, and 11 μm channel combinations; (middle row) 11–12 μm split window imagery; and (bottom row) the results of the SECO ash/dust detection algorithm using the 0.65, 3.9, 7.3, 8.5, 11, and 12 μm channel combinations are shown for all Aqua MODIS ascending (afternoon) node overpasses on 26 January 2011. The SECO results are displayed by overlaying the pixel-level probability of ash/dust over the 11 μm brightness temperature image in locations where the SECO algorithm detected ash or dust.

analyzed ROI, while the split window false alarms are located well outside of the ROI. The CSI of the SECO approach does decrease when less spectral channels are used, but not by a substantial amount.

5.3. South American Dust (Daytime)

When the complete SECO algorithm is applied to the South American suspended lake sediment case from P15, the SECO algorithm significantly improves upon the split window technique, except when the SC4 implementation is used (Figure 7). The SC4 channel combination results in no pixels being classified as dust, which illustrates the value of using additional spectral channels, especially over complicated land surfaces. There is essentially no difference between the SC1 and SC2 results, with both channel combinations having a CSI of 0.54. The FAR of the SC1 and SC2 results (2.03×10^{-3}), however, is larger compared to the Cleveland ash results because the western edge of the dust cloud is overestimated relative to the manual analysis. Errors in the clear-sky radiance calculations combined with surface emissivity effects lead to the westernmost cloud object being partially composed of pixels that are outside of the identifiable bounds of the dust cloud. No other false alarms were found, and the SC1 and SC2 FAR is still an order of magnitude smaller than the split window FAR. The SC3 implementation has a CSI of 0.50 with very few false alarms, all of which are located right along the boundary of the manually analyzed cloud. This case shows that the SECO method is effective over complicated land surfaces during sunlit conditions.

5.4. South American Dust (Nighttime)

In P15, a nocturnal South American dust cloud, generated by an outflow boundary, was analyzed. This same case is revisited using the complete SECO algorithm (Figure 8). The dust cloud in this scene has 11 μm BT values that deviate only slightly from the clear-sky values; therefore, this case is very challenging. As a result, only the SC1 and SC2 implementations of the SECO algorithm are able to detect any dust. The CSI of the SC1 implementation is more than 3 times greater than the split window, primarily due to the very low FAR of the SC1 implementation compared to the split window

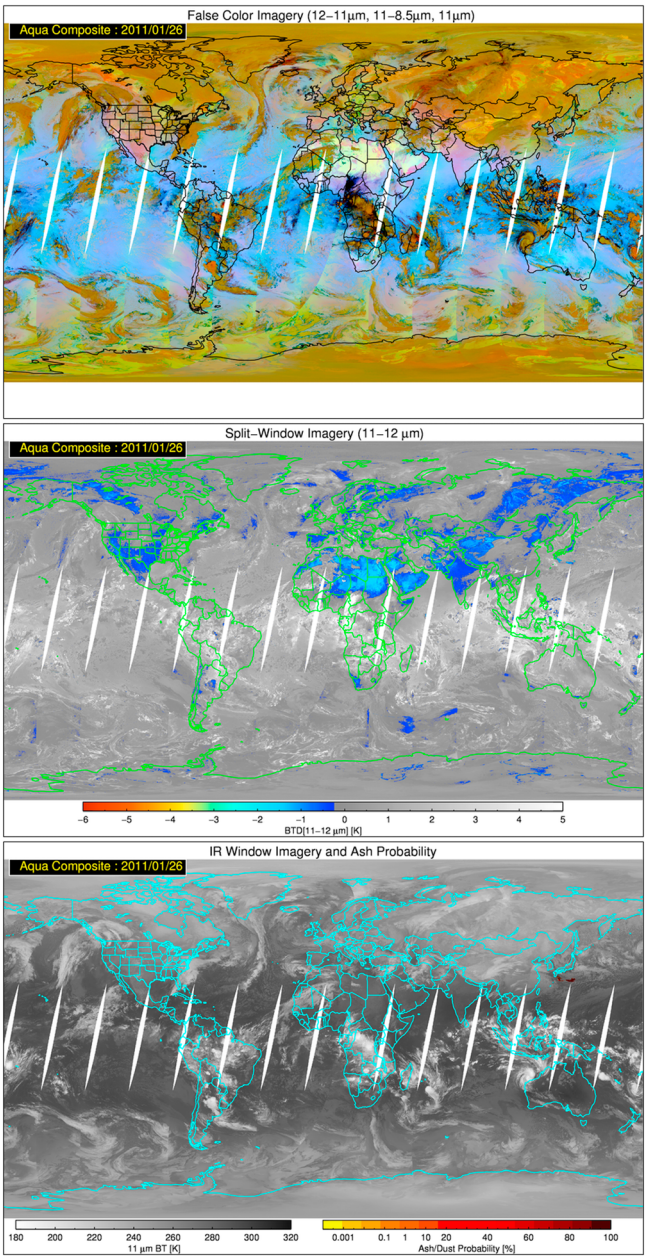

Figure 10. Same as Figure 9 except for all descending (overnight) Aqua MODIS overpasses on 26 January 2011.

technique. The SC2 implementation is only a slight improvement to the split window approach, but the much higher POD of the split window comes with a FAR that is 3 orders of magnitude greater than the SC2 FAR. Despite the severe detection deficiency of the SC3 and SC4 implementations, neither implementation produces any false alarms. Improvements to the cloud object selection procedure may lead to improved detection capabilities for all channel combinations.

6. Global Analysis

The skill score of the SECO method, with the full complement of spectral channels (the SC4 implementation), was assessed using a full day of *Aqua* MODIS data from 26 January 2011. All data from this day are independent of the training data set. On 26 January 2011 four volcanoes produced ash clouds that were identifiable in MODIS false color imagery. Kizimen and Karymsky volcanoes on the Kamchatka Peninsula of Russia and Sakurajima (Japan) produced small ash plumes that were identifiable in MODIS multispectral imagery. The existence of these plumes in MODIS false color imagery is consistent with the volcanic activity reported by the Smithsonian Global Volcanism Program (http://www.volcano.si.edu/reports_weekly.cfm#vn_300130). In addition, more significant ash emissions were produced by the eruption of Shinmoe-dake, a stratovolcano of the Kirishima volcano group in Japan [*Miyabuchi et al.*, 2013]. Mainly optically thin regions of African (Saharan) and Asian dust were also present in MODIS false color (and true color) imagery at times, but the horizontal bounds of the dust over the desert surface are difficult to determine; therefore, the 16 5 min MODIS granules (out of a total of 288) that possibly contained regions of dust were excluded from the skill score analysis. Thus, only the Kizimen, Karymsky, Sakurajima, and Shinmoe-dake ash clouds were manually analyzed.

The global ash detection results are visualized for both orbital nodes of Aqua MODIS in Figures 9 (ascending node) and 10 (descending node). The ascending node (Figure 9) consists primarily of sunlit observations (except at high latitudes in the Northern Hemisphere), and the descending node consists of nighttime observations (except at high latitudes in the Southern Hemisphere). In the ascending node, the SECO algorithm detects dust clouds over the Sahara and Asia. The presence of dust in these regions is confirmed in the false color imagery (especially when viewed close-up). No other regions of ash or dust are detected (no false alarms). However, the SECO algorithm does miss some areas of low optical depth dust over Africa

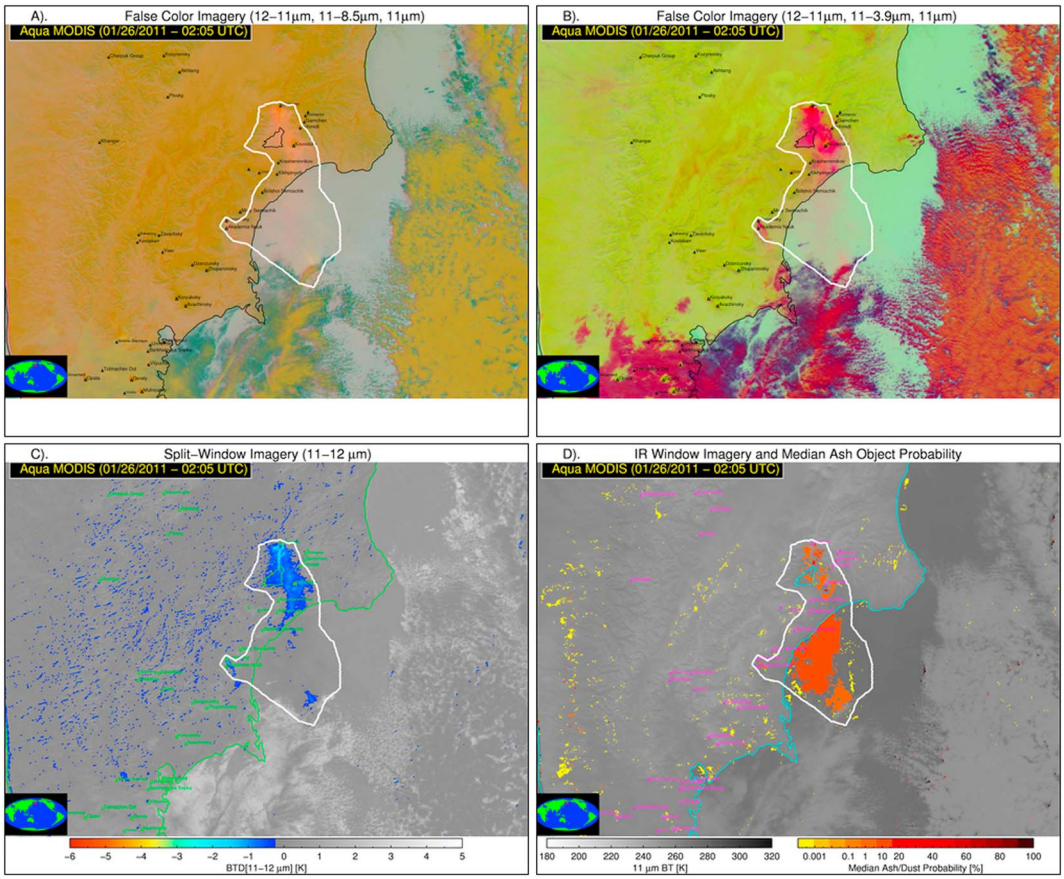

Figure 11. Volcanic ash plumes produced by eruptions of Kizimen and Karymsky on the Kamchatka Peninsula (Russia), which were captured by a daytime overpass of Aqua MODIS on 26 January 2011 (02:05 UTC), are examined in greater detail. (a) The 12–11, 11–8.5, and 11 μm false color image. (b) The 12–11, 11–3.9, and 11 μm false color image. (c) The 11–12 μm split window brightness temperature difference. (d) The median cloud object probability from the 0.65, 3.9, 7.3, 8.5, 11, and 12 μm implementation of the SECO algorithm overlaid on the corresponding 11 μm brightness image.

and Asia because the cloud objects associated with these low optical depth clouds did not exhibit the necessary spectral attributes to be chosen by the cloud object selection procedure. The SECO algorithm also misses weak ash plumes from Kizimen and Karymsky (Figure 11) for the same reason the low optical depth dust clouds are missed. The 11 μm brightness temperatures in the over land portion of the Kizimen and Karymsky plumes are very similar to the calculated clear-sky 11 μm brightness temperature. Thus, the cloud objects, denoted by the median cloud object probability, within the ROI in Figure 11d are not selected. No other volcanic ash clouds are present in the ascending node multispectral imagery. In the future, the detection of low optical depth ash/dust clouds or ash/dust clouds that exhibit very little thermal contrast with the estimated clear-sky brightness temperatures can potentially be improved through incorporation of information from multispectral satellite data collected at previous times or through incorporation of geometric properties (e.g., seek out plume-like objects or collections of objects).

In the descending node (Figure 10), the SECO algorithm detects ash clouds associated with the eruptions of Sakurajima (very minor ash emission) and Shinmoe-dake (more significant ash emission) in Japan. No other regions of volcanic ash or dust are detected. The volcanic ash clouds from the Japanese volcanoes are examined in greater detail (Figure 12). While the areal extent of the volcanic ash detected by the SECO algorithm is much smaller than the manually defined ROI (Figure 12d), the SECO algorithm does correctly detect ash in regions that do not exhibit a robust split window signature (Figure 12c). Portions of the ash cloud that overlap low meteorological clouds are missed, as are the optically thick (and perhaps ice topped) portions near Shinmoe-dake. The Sakurajima ash plume, which is detected by the SECO algorithm, is only composed of about 200 pixels and is barely noticeable in the far western part of

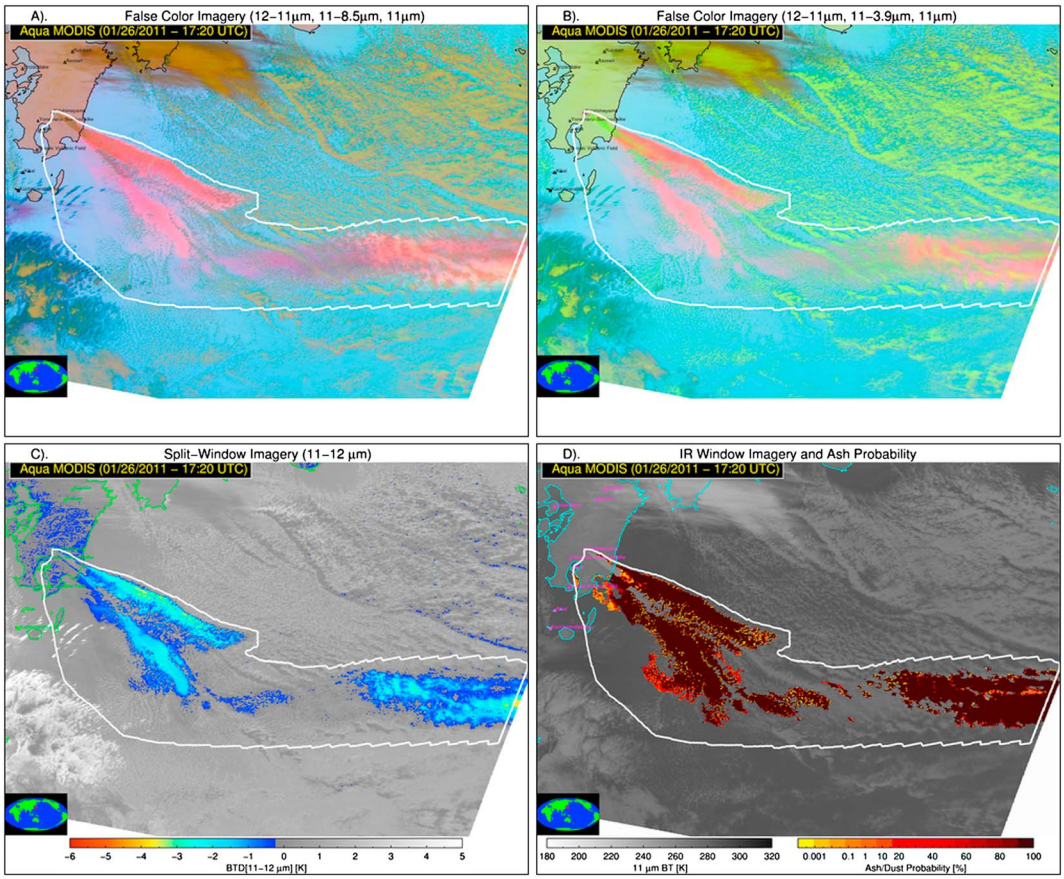

Figure 12. Volcanic ash produced by a minor emission from Sakurajima and a more significant emission from Shinmoe-dake in Japan, which was captured by a nighttime overpass of Aqua MODIS on 26 January 2011 (17:20 UTC), are examined in greater detail. (a) The 12–11, 11–8.5, and 11 μm false color image. (b) The 12–11, 11–3.9, and 11 μm false color image. (c) The 11–12 μm split window brightness temperature difference. (d) Volcanic ash detected by the 3.9, 7.3, 8.5, 11, and 12 μm implementation of the SECO algorithm is denoted by valid values of pixel-level ash/dust probability in lieu of the 11 μm brightness temperature value.

the images in Figure 12. Note that the SECO algorithm does not detect any volcanic ash outside of the ROI. An ash plume from Kizimen is also noticeable in multispectral imagery, albeit barely (Figure 13). The SECO algorithm does not detect the Kizimen ash plume, as it simply exhibits very little contrast with the surrounding environment, especially over land. The ROI does, however, contain a few cloud objects (Figure 13d), so this very weak plume can potentially be detected using a more sophisticated cloud object selection procedure.

Only excluding the 16 MODIS granules that contained diffuse dust clouds with ill-defined edges, the skill score of the SC1 implementation of the SECO algorithm and the split window approach were determined using the global 26 January 2011 Aqua MODIS data set. The results are shown in Figure 14. The SECO approach has a CSI that is more than 6 times greater than the split window technique. The split window ash/dust detection threshold was set at -1.70 K because that threshold resulted in the greatest CSI in this global analysis. The threshold of -1.70 K is exceptionally conservative, yet more than 20,000 false alarms are associated with the FAR of 5.4×10^{-5}. The SECO method only produced 20 false alarm pixels, all of which were located near the edge of the Japanese ash ROI. A total of about 736,982,000 pixels were included in this analysis. While the SECO POD (0.31) greatly exceeds the split window POD (0.07), the SECO POD is rather low. The low PODs can be attributed to the superior ability of the human expert to identify specific objects in images. Many of the additional regions of volcanic ash or dust identified by the human expert are extremely tenuous or are identified through spatial deduction. In addition, the small buffer applied when manually drawing the cloud edges to ensure that all ash/dust are encompassed by the ROI

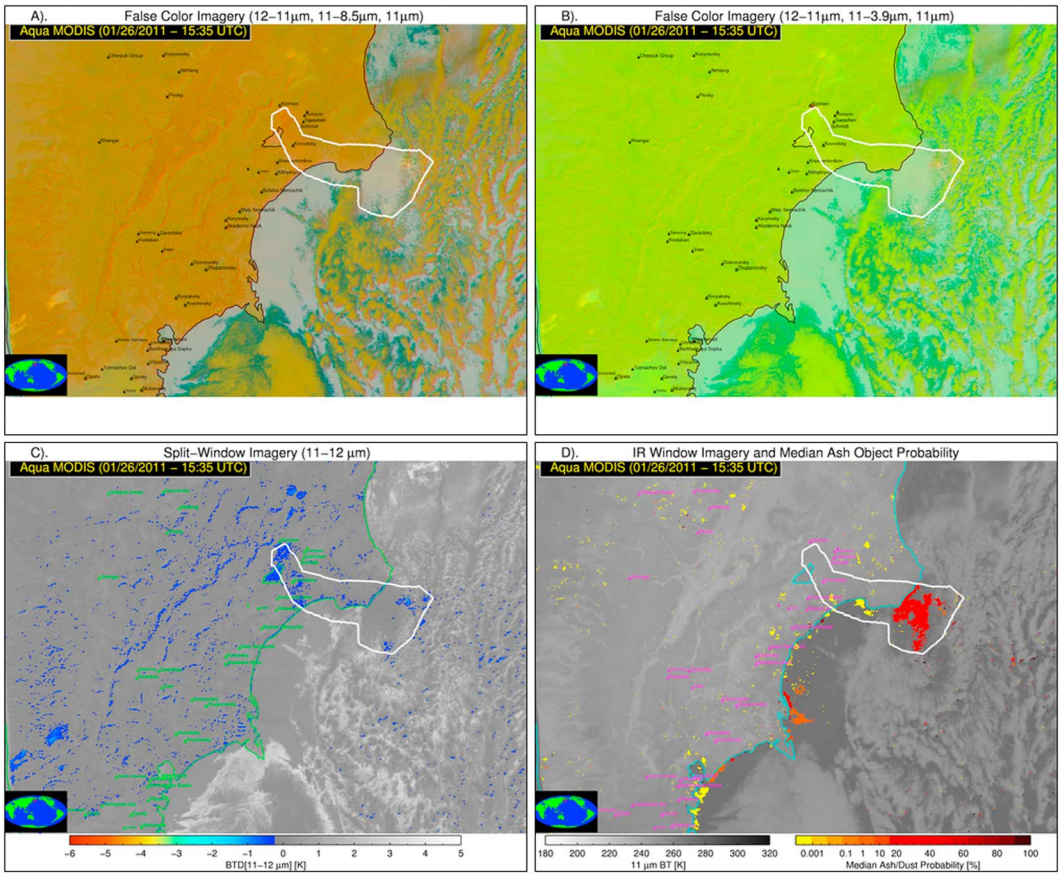

Figure 13. Same as Figure 11 except for a nighttime 26 January 2011 15:35 UTC Aqua MODIS overpass.

has a significant effect on the POD, especially for large clouds. The main goal of the skill score analyses is to quantitatively demonstrate that the SECO algorithm has a very low false alarm rate and significantly improves upon the traditional split window approach. Both of those goals have been achieved.

7. Sensor Intercomparison

In order to illustrate that the SECO method can be applied to nearly any sensor, the Shinmoe-dake ash cloud shown in Figure 12 was analyzed using the Multifunctional Transport Satellite (MTSAT), which is an

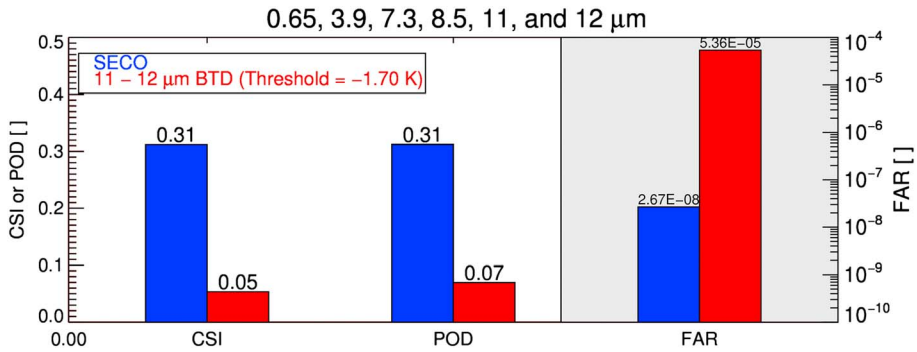

Figure 14. SECO and split window algorithm performance statistics (CSI, POD, and FAR) measured against manual analysis of multispectral imagery for an entire day of Aqua MODIS overpasses on 26 January 2011. Only MODIS granules that likely contain diffuse dust clouds with ill-defined edges are excluded. The SECO results, using the 0.65, 3.8, 7.3, 8.5, 11, and 12 μm channel combinations, are shown in blue, and the split window results obtained using the BTD(11–12 μm) threshold that produced the greatest CSI for this particular day of data are shown in red.

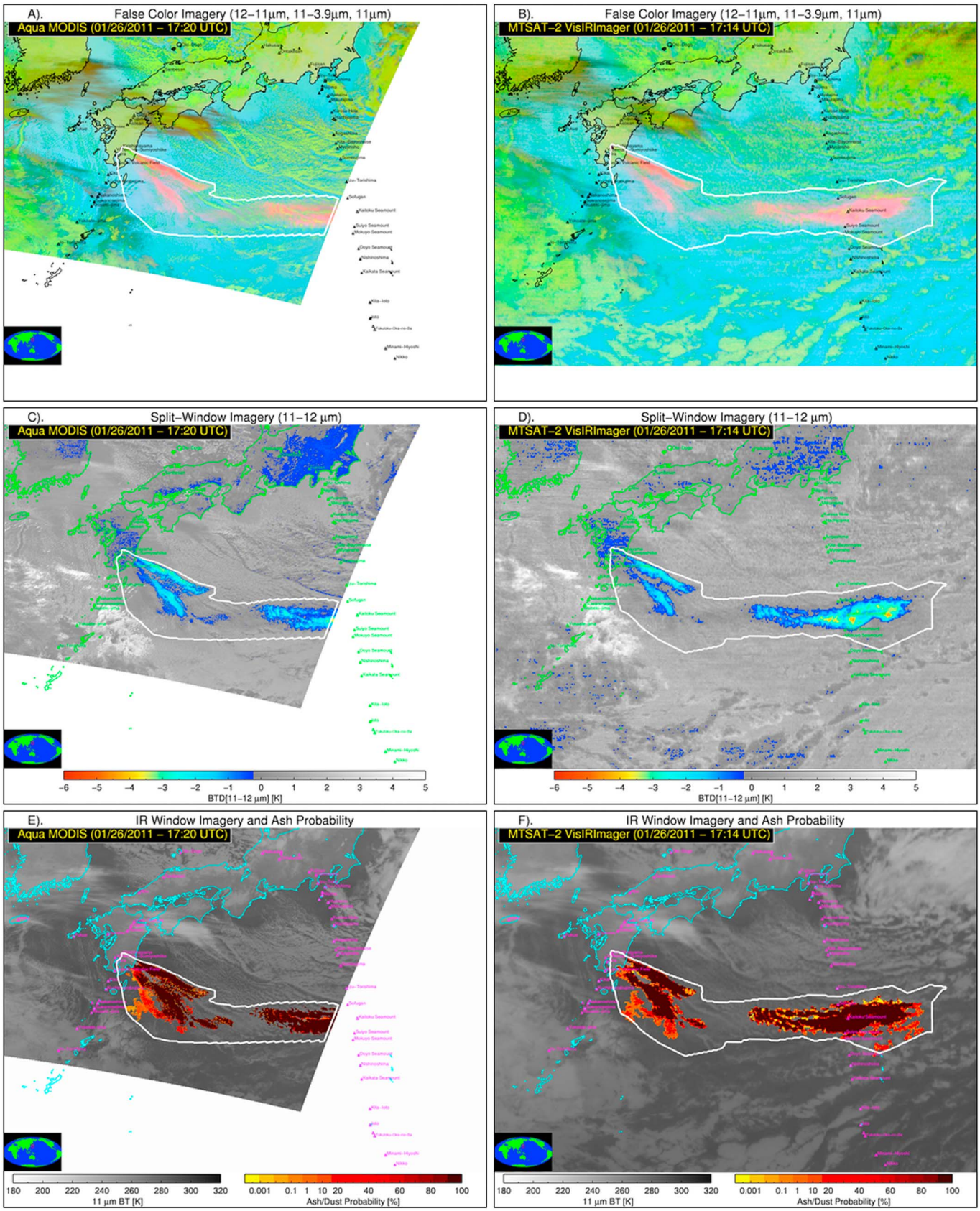
A). False Color Imagery (12–11μm, 11–3.9μm, 11μm)
Aqua MODIS (01/26/2011 – 17:20 UTC)
B). False Color Imagery (12–11μm, 11–3.9μm, 11μm)
MTSAT–2 VisIRImager (01/26/2011 – 17:14 UTC)
C). Split–Window Imagery (11–12 μm)
Aqua MODIS (01/26/2011 – 17:20 UTC)
D). Split–Window Imagery (11–12 μm)
MTSAT–2 VisIRImager (01/26/2011 – 17:14 UTC)
−6 −5 −4 −3 −2 −1 0 1 2 3 4 5
BTD[11–12 μm] [K]
E). IR Window Imagery and Ash Probability
Aqua MODIS (01/26/2011 – 17:20 UTC)
F). IR Window Imagery and Ash Probability
MTSAT–2 VisIRImager (01/26/2011 – 17:14 UTC)
180 200 220 240 260 280 300 320
11 μm BT [K]
0.001 0.1 1 10 20 40 60 80 100
Ash/Dust Probability [%]

Figure 15

operational geostationary meteorological satellite operated by the Japanese Meteorological Agency in the western Pacific at 145°E. MTSAT has a five-channel imager with spectral channels centered near 0.65, 3.9, 6.7, 11, and 12 μm. Thus, it allows for the SC3 implementation of the SECO approach. MTSAT has a nadir resolution of 4 km in the near infrared and infrared compared to MODIS, which has 1 km resolution in similar spectral channels. Many radiometric attributes (e.g., noise, instrument performance, and spectral response functions) of MODIS and MTSAT also differ. Given the differing orbital, spatial, spectral, and radiometric attributes between MTSAT and MODIS, MTSAT is a good sensor to use to determine if the SECO approach, which was trained using MODIS data, can be applied to other sensors with similar results when similar spectral channel combinations are utilized.

The 17:14 UTC MTSAT-2 scan of the Northern Hemisphere portion of the full disk was used to generate SECO algorithm results that can be compared to the 17:20 UTC MODIS overpass of the Shinmoe-dake ash cloud on 26 January 2011. The SC3 implementation of the SECO algorithm was applied to all Earth-located MTSAT-2 pixels in the Northern Hemisphere portion of the full disk. The only MTSAT pixels where ash or dust was detected by the SECO algorithm are associated with the Shinmoe-dake ash cloud. The Kizimen ash cloud shown in Figure 13 and the Sakurajima ash cloud shown in Figure 12 are very small scale features and, as such, are not identifiable in MTSAT imagery due to the very large MTSAT pixel size at larger viewing angles. Figure 15 shows how the MTSAT-based SECO detection of the Shinmoe-dake ash cloud compares with the MODIS-based SECO detection. The SC3 implementation of the SECO approach was used to generate both the MTSAT and MODIS results, and a ROI was manually constructed for both sensors (white contours in Figure 15). The MODIS results are shown in Figures 15a, 15c, and 15e, and the MTSAT results are shown in Figures 15b, 15d, and 15f. As Figure 15 shows, both the spatial coverage of detected ash and the ash probabilities are quite similar (note that the far eastern portion of the ash cloud falls outside of the MODIS swath shown in Figure 15). Most of the differences in ash probability are at cloud edges where differences in spatial resolution have the greatest impact. Using the ROIs, the CSI, POD, and FAR of the SC3 SECO implementation were computed for both sensors along with the corresponding split window statistics associated with the maximum possible CSI. For both MODIS and MTSAT the CSI was 0.40 with a FAR on the order of 10^{-6}. All of the SECO false alarms are located very close to the manually analyzed ash cloud boundary. The split window method has a CSI of 0.16 and a FAR of 0.005 when a threshold of −0.7 K is applied to MODIS. When applied to MTSAT, the maximum split window CSI is 0.09 with a FAR of 0.002 using a threshold of −1.4 K. Unlike the SECO results, nearly all of the split window false alarms occur well outside the bounds of the manually analyzed ash cloud. This example illustrates that the SECO approach can produce results that are consistent across sensors, even when the split window-based detection is not.

8. Summary and Conclusions

The SECO algorithm combines radiative transfer theory, Bayesian methods, and image processing/computer vision concepts to identify volcanic ash and dust clouds in multispectral satellite data with skill that is more comparable to a human expert than the traditional split window technique. The volcanic ash/dust probability determined using the naïve Bayesian approach described in *Pavolonis et al*. [2015], in combination with results from a cloud property retrieval algorithm [*Pavolonis et al*., 2013], is used to identify satellite pixels that might contain volcanic ash and/or dust. All pixels that potentially contain ash or dust are sorted into cloud objects. A cloud object is a collection of spatially connected satellite pixels that meet a specified set

Figure 15. Volcanic ash produced by a minor emission from Sakurajima and a more significant emission from Shinmoe-dake in Japan, which was captured by Aqua MODIS on 26 January 2011 (17:20 UTC) and MTSAT on 26 January 2011 (17:15 UTC), are shown. (a) The 12–11, 11–3.9, and 11 μm false color image from MODIS. (b) The 12–11, 11–3.9, and 11 μm false color image from MTSAT. (c) The 11–12 μm split window brightness temperature difference from MODIS. (d) The 11–12 μm split window brightness temperature difference from MTSAT. (e) Volcanic ash detected by the 3.9, 11, and 12 μm implementation of the SECO algorithm applied to MODIS is denoted by valid values of pixel-level ash/dust probability in lieu of the 11 μm brightness temperature value. (f) Volcanic ash detected by the 3.9, 11, and 12 μm implementation of the SECO algorithm applied to MTSAT is denoted by valid values of pixel-level ash/dust probability in lieu of the 11 μm brightness temperature value. The images were taken at night.

of criteria. An ash/no ash (or dust/no dust) classification is then assigned on a cloud object basis. The majority of volcanic ash and dust clouds are composed of a small subset of pixels that are spectrally unique (e.g., very unlikely to be associated with any other feature) and a larger subset of pixels that, to varying degrees, are spectrally nonunique (e.g., can sometimes be associated with other features). In essence, a cloud object is assigned to the volcanic ash/dust class if the object contains a specified number of pixels that exhibit a spectral signature that is unambiguously associated with volcanic ash or dust (volcanic ash and dust exhibit very similar spectral signatures in weather satellite data). The resulting pixel-level ash/no ash (or dust/no dust) classification is used to screen out any ash cloud property retrievals that were performed outside of volcanic ash or dust clouds.

The SECO method is globally applicable and can be applied to virtually any low Earth orbit or geostationary satellite sensor. Further, the SECO approach was quantitatively proven to be more skillful than the commonly used split window technique. More specifically, the SECO method has a much higher probability of detection than the traditional split window method while maintaining a near-zero false alarm rate. Comparisons to additional ash/dust detection methods, including those derived from lidar [e.g., *Liu et al*., 2008] and passive ultraviolet [e.g., *de Graaf et al*., 2005] and visible [e.g., *Hsu et al*., 2013] observations, will be performed in the future, as the primary goal of this paper and *Pavolonis et al*. [2015] was to introduce the SECO method and demonstrate that it is globally applicable and general enough to be applied to low Earth orbit and geostationary passive satellite sensors with differing measurement capabilities.

Several additions to the SECO approach can be made to increase the probability of detection while maintaining an exceptionally low false alarm rate. For instance, ash/dust cloud objects can be tracked in time, thereby allowing very low cloud optical depth ash/dust cloud objects to be selected on the basis of a priori information on the geographic location of ash/dust. In addition, geometric properties can be used to identify cloud objects or collections of cloud objects that have a plume-like shape that originates near a volcano. Finally, cloud vertical growth information [*Cintineo et al*., 2013] can be combined with spectral information to improve the detection of optically thick clouds that contain volcanic ash. Current and future research is focused on developing these additional components for integration into the basic SECO approach. Discrimination of ash and dust is also important and will be a focus of future SECO development efforts.

Appendix A

Cloud object membership is granted to a given satellite pixel if the ash/dust posterior probability [$P(C_{yes}|\mathbf{F})$] exceeds *any* of the five thresholds defined by equations (A1) and (A3)–(A6). The first probability threshold ($P_{thresh1}$) is determined through sequential evaluation of the conditions listed in equation (A1) (the evaluation stops once a true condition on the right-hand side is encountered). In equation (A1), $\varepsilon_{tot}(11\ \mu m)$ is the 11 μm top of troposphere emissivity (see main text), $\varepsilon_{err}(11\ \mu m)$ is the 11 μm ash/dust cloud emissivity retrieval uncertainty divided by the first guess uncertainty, and BTD(11–12 μm) is the 11–12 μm brightness temperature difference.

$$P_{thresh1}\begin{cases} 1\%, & \varepsilon_{tot}(11\ \mu m) \geq 0.25 \text{ or BTD}(11-12\ \mu m) < -0.5\ \text{K} \\ 1\%, & \varepsilon_{err}(11\ \mu m) \leq 0.40 \\ 5\%, & 0.40 < \varepsilon_{err}(11\ \mu m) \leq 0.50 \\ 10\%, & 0.50 < \varepsilon_{err}(11\ \mu m) \leq 0.70 \\ 90\%, & 0.70 < \varepsilon_{err}(11\ \mu m) \leq 0.90 \\ 95\%, & \text{otherwise} \end{cases} \tag{A1}$$

The second probability threshold ($P_{thresh2}$) depends on the difference between the BTD(11–12 μm) at the pixel of interest (BTD_o) and the mean BTD(11–12 μm) at locations within 25 km that have a $P(C_{yes}|\mathbf{F})$ that is less than $1.0e^{-6}$% (BTD_{region}) and a $\varepsilon_{tot}(11\ \mu m)$ that differs by no more than one third of the $\varepsilon_{tot}(11\ \mu m)$ value at the pixel of interest. Absolute [$DBTD_{abs} = BTD_{region} - BTD_o$] and relative [$DBTD_{rel} = (BTD_{region} - BTD_o)/BTD_{region}$] differences are computed, and a decision tree equivalent to equation (A2),

evaluated in sequential order (the evaluation stops once a true condition on the right-hand side is encountered), is executed.

$$\text{Condition2} = \begin{cases} \text{False}, & \text{BTD}(11-12\ \mu\text{m}) > 2.0\ \text{K} \\ \text{False}, & \varepsilon_{\text{tot}}(11\ \mu\text{m}) < 0.001\ \text{or}\ \varepsilon_{\text{tot}}(11\ \mu\text{m}) > 0.25 \\ \text{False}, & \varepsilon(11\ \mu\text{m}) > 0.50 \\ \text{False}, & \text{BT}_{\text{sdev}}(11\ \mu\text{m}) > 2.0\ \text{K} \\ \text{False}, & N_{25\text{km}} < 5 \\ \text{False}, & \text{DBTD}_{\text{abs}} < 0.25\ \text{K} \\ \text{True}, & \text{DBTD}_{\text{rel}} < 0.25\ \text{K and}\ \varepsilon_{\text{err}}(11\ \mu\text{m}) < 0.30 \\ \text{True}, & \text{DBTD}_{\text{rel}} < 0.30\ \text{K and}\ \varepsilon_{\text{err}}(11\ \mu\text{m}) < 0.35 \\ \text{True}, & \text{DBTD}_{\text{rel}} < 0.35\ \text{K and}\ \varepsilon_{\text{err}}(11\ \mu\text{m}) < 0.40 \\ \text{True}, & \text{DBTD}_{\text{rel}} < 0.40\ \text{K and}\ \varepsilon_{\text{err}}(11\ \mu\text{m}) < 0.45 \\ \text{True}, & \text{DBTD}_{\text{rel}} < 0.45\ \text{K and}\ \varepsilon_{\text{err}}(11\ \mu\text{m}) < 0.50 \\ \text{True}, & \text{DBTD}_{\text{rel}} < 0.50\ \text{K and}\ \varepsilon_{\text{err}}(11\ \mu\text{m}) < 0.55 \\ \text{True}, & \text{DBTD}_{\text{rel}} < 0.55\ \text{K and}\ \varepsilon_{\text{err}}(11\ \mu\text{m}) < 0.60 \\ \text{True}, & \text{DBTD}_{\text{rel}} < 0.60\ \text{K and}\ \varepsilon_{\text{err}}(11\ \mu\text{m}) < 0.65 \\ \text{True}, & \text{DBTD}_{\text{rel}} < 0.65\ \text{K and}\ \varepsilon_{\text{err}}(11\ \mu\text{m}) < 0.70 \\ \text{True}, & \text{DBTD}_{\text{rel}} < 0.70\ \text{K and}\ \varepsilon_{\text{err}}(11\ \mu\text{m}) < 0.75 \\ \text{True}, & \text{DBTD}_{\text{rel}} < 0.75\ \text{K and}\ \varepsilon_{\text{err}}(11\ \mu\text{m}) < 0.80 \\ \text{True}, & \text{DBTD}_{\text{rel}} < 0.80\ \text{K and}\ \varepsilon_{\text{err}}(11\ \mu\text{m}) < 0.85 \\ \text{True}, & \text{DBTD}_{\text{rel}} < 0.85\ \text{K and}\ \varepsilon_{\text{err}}(11\ \mu\text{m}) < 0.90 \\ \text{False}, & \text{Otherwise} \end{cases} \tag{A2}$$

In equation (A2), $\varepsilon(11\ \mu\text{m})$ is the retrieved ash/dust cloud emissivity at 11 μm, $\text{BT}_{\text{sdev}}(11\ \mu\text{m})$ is the standard deviation of the 11 μm brightness temperature in a 3×3 pixel window centered on the pixel of interest, and $N_{25\text{km}}$ is the number of pixels used to compute DBTD_{abs} and DBTD_{rel}. The second cloud object membership (P_{thresh2}) threshold is then determined using the relationship shown in equation (A3).

$$P_{\text{thresh2}} = \begin{cases} 0.001\%, & \text{if Condition2 is true} \\ 100\%, & \text{otherwise} \end{cases} \tag{A3}$$

The third probability threshold (P_{thresh3}) is determined through sequential evaluation of equation (A4) (the evaluation stops once a "true" condition on the right-hand side is encountered).

$$P_{\text{thresh3}} = \begin{cases} 100\%, & \text{if}\ \varepsilon_{\text{tot}}(11\ \mu\text{m}) < 0.05 \\ 100\%, & \text{if BTD}(11-12\ \mu\text{m}) > -0.50 \\ 0.00\%, & \text{if BTD}_{\text{BIAS}} > -1.50\ \text{K} \\ 0.00\%, & \text{if BTD}_{\text{BIAS}} > -1.00\ \text{K and}\ 0.30 \le \varepsilon(11\ \mu\text{m}) \le 0.70 \\ 0.0001\%, & \text{if BTD}_{\text{BIAS}} > -1.00\ \text{K} \\ 100\%, & \text{otherwise} \end{cases} \tag{A4}$$

The fourth probability threshold (P_{thresh4}), given by equation (A5), is designed to account for the presence of SO_2, which is common in volcanic eruptions. In equation (A5), $\beta_{\text{tot}}(8.5\ \mu\text{m}, 11\ \mu\text{m})$, $\beta_{\text{opaque}}(8.5\ \mu\text{m}, 11\ \mu\text{m})$, and $\beta_{\text{tot}}(7.3\ \mu\text{m}, 11\ \mu\text{m})$ are SO_2 sensitive formulations of the β ratio discussed in detail in *Pavolonis et al.* [2015].

$$P_{\text{thresh4}} = \begin{cases} 1.0e^{-8}\%, & \text{if } \beta_{\text{tot}}(8.5\ \mu\text{m}, 11\ \mu\text{m}) > 1.50 \text{ and} \\ & \beta_{\text{opaque}}(8.5\ \mu\text{m}, 11\ \mu\text{m}) > 2.50 \text{ and} \\ & \beta_{\text{tot}}(7.3\ \mu\text{m}, 11\ \mu\text{m}) > 1.0 \text{ and} \\ & \varepsilon_{\text{tot}}(11\ \mu\text{m}) > 0.01 \\ 100\,\%, & \text{otherwise} \end{cases} \tag{A5}$$

The fifth and final probability threshold (P_{thresh5}) simply depends on the retrieved ash/dust mass loading (ML) (see equation (A6)).

$$P_{\text{thresh5}} = \begin{cases} 1.0e^{-13}\%, & \text{if ML} < 1\text{g/m}^2 \\ 100\%, & \text{otherwise} \end{cases} \tag{A6}$$

Acknowledgments
NOAA GOES-R Risk Reduction funded this research. The MODIS data utilized in this study are freely available from the NASA Level 1 and Atmosphere Archive and Distribution System (LAADS) at http://ladsweb.nascom.nasa.gov/. The MTSAT-2 data are available from the Space Science and Engineering Center (SSEC) Data Center at http://www.ssec.wisc.edu/datacenter/archive.html. The software utilized to generate the results described in this paper is available upon request by sending an email to Mike.Pavolonis@noaa.gov. We thank Fred Prata and an anonymous reviewer for helping improve the quality of the manuscript. The views, opinions, and findings contained in this report are those of the author(s) and should not be construed as an official National Oceanic and Atmospheric Administration or U.S. Government position, policy, or decision.

References

Cintineo, J. L., M. Pavolonis, and J. Sieglaff (2013), Evolution of severe and nonsevere convection inferred from GOES-derived cloud properties, *J. Appl. Meteorol. Climatol.*, *52*(9), 2009–2023.

de Graaf, M., P. Stammes, O. Torres, and R. Koelemeijer (2005), Absorbing Aerosol Index: Sensitivity analysis, application to GOME and comparison with TOMS, *J. Geophys. Res.*, *110*, D01201, doi:10.1029/2004JD005178.

Heidinger, A., and M. Pavolonis (2009), Gazing at cirrus clouds for 25 years through a split window. Part I: Methodology, *J. Appl. Meteorol. Climatol.*, *48*(6), 1100–1116, doi:10.1175/2008JAMC1882.1.

Heidinger, A. K., A. T. Evan, M. J. Foster, and A. Walther (2012), A naive Bayesian cloud-detection scheme derived from CALIPSO and applied within PATMOS-x, *J. Appl. Meteorol. Climatol.*, *51*(6), 1129–1144, doi:10.1175/jamc-d-11-02.1.

Hsu, N. C., M. J. Jeong, C. Bettenhausen, A. M. Sayer, R. Hansell, C. S. Seftor, J. Huang, and S. C. Tsay (2013), Enhanced Deep Blue aerosol retrieval algorithm: The second generation, *J. Geophys. Res. Atmos.*, *118*, 9296–9315, doi:10.1002/jgrd.50712.

Lensky, I., and D. Rosenfeld (2008), Clouds-Aerosols-Precipitation Satellite Analysis Tool (CAPSAT), *Atmos. Chem. Phys.*, *8*(22), 6739–6753.

Liu, D., Z. Wang, Z. Liu, D. Winker, and C. Trepte (2008), A height resolved global view of dust aerosols from the first year CALIPSO lidar measurements, *J. Geophys. Res.*, *113*, D16214, doi:10.1029/2007JD009776.

Miyabuchi, Y., D. Hanada, H. Niimi, and T. Kobayashi (2013), Stratigraphy, grain-size and component characteristics of the 2011 Shinmoedake eruption deposits Kirishima Volcano, Japan, *J. Volcanol. Geotherm. Res.*, *258*, 31–46, doi:10.1016/j.jvolgeores.2013.03.027.

Pavolonis, M. (2010), Advances in extracting cloud composition information from spaceborne infrared radiances—A robust alternative to brightness temperatures. Part I: Theory, *J. Appl. Meteorol. Climatol.*, *49*(9), 1992–2012, doi:10.1175/2010JAMC2433.1.

Pavolonis, M., W. Feltz, A. Heidinger, and G. Gallina (2006), A daytime complement to the reverse absorption technique for improved automated detection of volcanic ash, *J. Atmos. Oceanic Technol.*, *23*(11), 1422–1444, doi:10.1175/JTECH1926.1.

Pavolonis, M., A. Heidinger, and J. Sieglaff (2013), Automated retrievals of volcanic ash and dust cloud properties from upwelling infrared measurements, *J. Geophys. Res. Atmos.*, *118*, 1436–1458, doi:10.1002/jgrd.50173.

Pavolonis, M. J. (2014), Development of satellite remote sensing techniques for quantifying volcanic ash cloud properties, PhD dissertation, 279 pp., Univ. of Wis-Madison, Madison. [Available at http://depot.library.wisc.edu.ezproxy.library.wisc.edu/repository/fedora/1711.dl:7M4TFYMUM5Z5Z8N/datastreams/REF/content.]

Pavolonis, M. J., J. Sieglaff, and J. Cintineo (2015), Spectrally Enhanced Cloud Objects—A generalized framework for automated detection of volcanic ash and dust clouds using passive satellite measurements: 1. Multispectral analysis, *J. Geophys. Res. Atmos.*, *120*, doi:10.1002/2014JD022968.

Prata, A. J. (1989a), Observations Of volcanic ash clouds in the 10–12 μM window using AVHRR/2 data, *Int. J. Remote Sens.*, *10*(4–5), 751–761.

Prata, A. J. (1989b), Infrared radiative transfer calculations for volcanic ash clouds, *Geophys. Res. Lett.*, *16*(11), 1293–1296, doi:10.1029/GL016i011p01293.

Wielicki, B. A., and R. M. Welch (1986), Cumulus cloud properties derived using Landsat satellite data, *J. Climate Appl. Meteorol.*, *25*(3), 261–276, doi:10.1175/1520-0450.